Article

Frontostriatal salience network expansion in individuals in depression

https://doi.org/10.1038/s41586-024-07805-2

Received: 2 August 2023

Accepted: 9 July 2024

Published online: 4 September 2024

Open access

Check for updates

Charles J. Lynch[1]✉, Immanuel G. Elbau[1], Tommy Ng[1], Aliza Ayaz[1], Shasha Zhu[1], Danielle Wolk[1], Nicola Manfredi[1], Megan Johnson[1], Megan Chang[1], Jolin Chou[1], Indira Summerville[1], Claire Ho[1], Maximilian Lueckel[2,3], Hussain Bukhari[1], Derrick Buchanan[4], Lindsay W. Victoria[1], Nili Solomonov[1], Eric Goldwaser[1], Stefano Moia[5,6,7], Cesar Caballero-Gaudes[7], Jonathan Downar[8], Fidel Vila-Rodriguez[9], Zafiris J. Daskalakis[10], Daniel M. Blumberger[8,11,12], Kendrick Kay[13], Amy Aloysi[14], Evan M. Gordon[15], Mahendra T. Bhati[4], Nolan Williams[4], Jonathan D. Power[1], Benjamin Zebley[1], Logan Grosenick[1], Faith M. Gunning[1] & Conor Liston[1]✉

Decades of neuroimaging studies have shown modest differences in brain structure and connectivity in depression, hindering mechanistic insights or the identification of risk factors for disease onset[1]. Furthermore, whereas depression is episodic, few longitudinal neuroimaging studies exist, limiting understanding of mechanisms that drive mood-state transitions. The emerging field of precision functional mapping has used densely sampled longitudinal neuroimaging data to show behaviourally meaningful differences in brain network topography and connectivity between and in healthy individuals[2–4], but this approach has not been applied in depression. Here, using precision functional mapping and several samples of deeply sampled individuals, we found that the frontostriatal salience network is expanded nearly twofold in the cortex of most individuals with depression. This effect was replicable in several samples and caused primarily by network border shifts, with three distinct modes of encroachment occurring in different individuals. Salience network expansion was stable over time, unaffected by mood state and detectable in children before the onset of depression later in adolescence. Longitudinal analyses of individuals scanned up to 62 times over 1.5 years identified connectivity changes in frontostriatal circuits that tracked fluctuations in specific symptoms and predicted future anhedonia symptoms. Together, these findings identify a trait-like brain network topology that may confer risk for depression and mood-state-dependent connectivity changes in frontostriatal circuits that predict the emergence and remission of depressive symptoms over time.

Depression is a heterogeneous and episodic neuropsychiatric syndrome associated with synapse loss[5,6] and connectivity alterations in frontostriatal networks[7–9] and a leading cause of disability worldwide[10]. The neurobiological mechanisms that give rise to specific depressive symptom domains or to changes in mood over time are not well understood, especially at the neural systems level. So far, most functional magnetic resonance imaging (fMRI) studies have tested for differences in functional connectivity in cross-sectional comparisons between groups of depressed individuals and healthy, never-depressed controls using group-average (one-size-fits-all) parcellations to define functional brain areas and networks. More recently, pioneering work in systems neuroscience has given rise to the field of precision functional mapping, which refers to a suite of new approaches for delineating functional networks entirely in individuals[2–4,11–14]. Precision mapping studies have shown that the topology (size, shape and spatial location) of functional areas and networks in individuals deviates markedly from group-average descriptions[3,15,16] and that individual differences in network topology are stable[2,3,17,18], heritable[19,20] and associated with cognitive abilities and behaviour[3–5,13,21–23]. Apart from a recent case study involving a single individual who sustained bilateral perinatal strokes[24], these tools have not yet been widely applied in clinical populations, including depression. Thus, whether

[1]Department of Psychiatry, Weill Cornell Medicine, New York, NY, USA. [2]Leibniz Institute for Resilience Research, Mainz, Germany. [3]Neuroimaging Center (NIC), Focus Program Translational Neurosciences (FTN), Johannes Gutenberg University Medical Center, Mainz, Germany. [4]Department of Psychiatry and Behavioral Sciences, Stanford University, Stanford, CA, USA. [5]Neuro-X Institute, École Polytechnique Fédérale de Lausanne, Geneva, Switzerland. [6]Department of Radiology and Medical Informatics, Faculty of Medicine, University of Geneva, Geneva, Switzerland. [7]Basque Center on Cognition, Brain and Language, Donostia, Spain. [8]Department of Psychiatry and Institute of Medical Science, University of Toronto, Toronto, Ontario, Canada. [9]Department of Psychiatry, University of British Columbia, Vancouver, British Columbia, Canada. [10]Department of Psychiatry, University of California, San Diego, CA, USA. [11]Temerty Centre for Therapeutic Brain Intervention, Toronto, Ontario, Canada. [12]Centre for Addiction and Mental Health, Toronto, Ontario, Canada. [13]Center for Magnetic Resonance Research, University of Minnesota, Minneapolis, MN, USA. [14]Icahn School of Medicine at Mount Sinai, New York, NY, USA. [15]Department of Radiology, Washington University School of Medicine, St. Louis, MO, USA. ✉e-mail: cjl2007@med.cornell.edu; col2004@med.cornell.edu

functional network topology differs in individuals with depression is unknown.

Depression is a fundamentally episodic neuropsychiatric condition defined by discrete periods of low mood interposed between periods of euthymia but our understanding of the mechanisms that mediate mood transitions over time is limited. This is due in part to the fact that most studies until now have been cross-sectional, involving data acquired at a single time point or, in some cases, two or three scans acquired before and after an intervention[25–27]—an approach that is not designed for meaningful statistical inferences at the individual level[21]. Understanding the neurobiological mechanisms that mediate transitions in and out of depressive mood states may require studying individual patients over many months[22]. Indeed, densely sampled *n*-of-1 studies involving intracranial EEG recordings and other assessments have begun to show mechanisms that regulate mood-state transitions in individual patients receiving deep brain stimulation for depression[23,28,29] but these approaches have not yet been deployed at scale in fMRI studies. Without such datasets, it is unknown whether changes in brain network connectivity predict the emergence of anhedonia, anxiety and dysfunction in other depressive symptom domains or the subsequent remission of these symptoms after a recovery from an episode. In the same way, it is unclear whether atypical network topology measures fluctuate with mood state in individuals with depression or remain stable over time—key questions for understanding cause-and-effect relationships in clinical neuroimaging, for defining potential therapeutic targets in neuromodulation interventions or identifying at-risk individuals. Until recently, technical limitations have posed significant obstacles to performing precision functional mapping and longitudinal neuroimaging in clinical samples, including depression. Conventional fMRI measurements at the single subject level are often noisy and have limited reliability, in part because they are sensitive to a variety of imaging artefacts[30]. However, recent studies have taken significant steps towards developing solutions to these problems, by either acquiring large quantities of data in each subject[2,3,14] or by using multi-echo fMRI[18,31]. Together, these approaches can generate highly reliable functional connectivity measures and network maps at the level of individual subjects, an important step towards developing and deploying fMRI for clinical translational purposes.

Here we used state-of-the-art precision functional mapping tools to delineate topology of functional brain networks in individuals with depression, leveraging several resting-state fMRI datasets of deeply sampled individuals. We found that the frontostriatal salience network is expanded by nearly twofold in most individuals with depression—an effect we replicated thrice using independent samples of repeatedly sampled individuals with depression (total $n = 135$) and in large-scale group-average data ($n = 299$ individuals with depression, $n = 932$ healthy controls), with three distinct types of encroachment displacing neighbouring functional systems occurring across individuals. Salience network expansion was stable over time and unaffected by changes in mood state. It was also present in children scanned before the onset of depression symptoms that emerged later in adolescence. Longitudinal analyses of densely sampled individuals showed mood-state-dependent changes in striatal connectivity with anterior cingulate and anterior insular nodes of the salience network which tracked fluctuations in anhedonia and anxiety, respectively, and predicted the subsequent emergence of anhedonic symptoms at future study visits.

Salience network expansion in depression

Numerous neuroimaging studies involving large cohorts of patients with depression have identified differences in functional connectivity and brain structure[32–36], often involving the anterior cingulate cortex, orbitofrontal cortex, insular cortex and subgenual cingulate cortex—a therapeutic target for deep brain stimulation[37,38]—but the effect sizes in large-scale meta-analyses are modest (for example, Cohen's $d = 0.1–0.15$ for structural measures[36] and $d = 0.13–0.26$ for functional connectivity measures[1]). Whether the topological features of large-scale functional brain networks—their shape, spatial location and size—are altered in depression is unknown.

We used precision functional mapping to delineate the topology of functional brain networks in six highly sampled individuals with unipolar major depression who underwent on average 621.5 min of multi-echo fMRI scanning (range 58–1,792 min) across 22 sessions (range 2–62 sessions). We refer to this dataset as the serial imaging of major depression (SIMD) dataset (study design and aims in Extended Data Fig. 1). To contextualize the severity of depressive symptoms in these individuals, the mean 17-item[39] Hamilton depression rating scale (HDRS17) score (averaged across study visits, excluding those when these individuals were in remission) was 15.7 ± 3.7 (range 10.5–22.2), indicating a range of severity levels from mild to severe. The same precision mapping procedures were applied to 37 highly sampled healthy controls with an average of 327.49 min of fMRI data per subject (range 43.36–841.2 min) across 12 sessions (range 2–84 sessions). The healthy controls did not receive any intervention or treatment. See the Methods for more details.

It was immediately apparent on visual inspection that the salience network, which is involved in reward processing and conscious integration of autonomic feedback and responses with internal goals and environmental demands[30,40,41], was markedly larger in these individuals with depression (Fig. 1a,b). In four of the six individuals, the salience network was expanded more than twofold, outside the range observed in all 37 healthy controls (Fig. 1c, left). On average, the salience network occupied 73% more of the cortical surface relative to the mean in healthy controls (5.49% ± 0.76% of cortex in SIMD versus 3.17% ± 0.85% of cortex in healthy controls), giving rise to a large group-level effect (Cohen's $d = 1.99$). This effect was replicated using an alternative network parcellation algorithm[42] (Supplementary Fig. 1) and without use of global signal regression (Supplementary Fig. 2), indicating that it is robust to methodological variation and was not explained by group differences in brain anatomy or structure (Supplementary Fig. 3) or head motion (independent sample *t*-test comparing mean framewise displacement, $T = 0.73$, $P = 0.47$, claims about equivalence are based on an absence of evidence).

To further validate this finding, we repeated this procedure in three samples ($n = 48$ and $n = 45$ from Weill Cornell Medicine and $n = 42$ from Stanford University) of individuals with depression. Detailed imaging, demographic and clinical information for these samples are available in Supplementary Table 1 and Supplementary Fig. 4. The effect was replicated thrice (Fig. 1c, right), again with medium to large effect sizes (Cohen's $d = 0.77–0.84$), remained statistically significant when controlling for the sex ratio imbalance in our samples (56.7% of individuals with depression were female, versus 31% of the healthy controls; Supplementary Fig. 4 and Extended Data Fig. 2) and with or without correction for potential site- or scanner-induced biases (Supplementary Fig. 5). We also evaluated if representation of the salience network was similarly increased in the striatum, which is thought to relate to anatomically well-defined, interconnected loops in which the cortex projects to the striatum and the striatum projects back to cortex indirectly through the thalamus[43,44] but found that the difference in group means was not statistically significant (Fig. 1d).

Salience network expansion in depression was also evident in density maps (Fig. 1e), which convey the percentage of individuals with salience network representation at each cortical vertex or striatal voxel. These maps confirmed a similar overall pattern of cortical and subcortical representation in both groups, consistent with descriptions in previous reports[3,45,46] but also showed that the borders of the salience network frequently extended further outwards from their centroids in each cortical zone in depressed individuals. For example, in the anterior cingulate cortex, network borders shifted more anteriorly into the pregenual cortex and, in lateral prefrontal cortex, network borders shifted more anteriorly towards the frontal pole (red boxes in Fig. 1e).

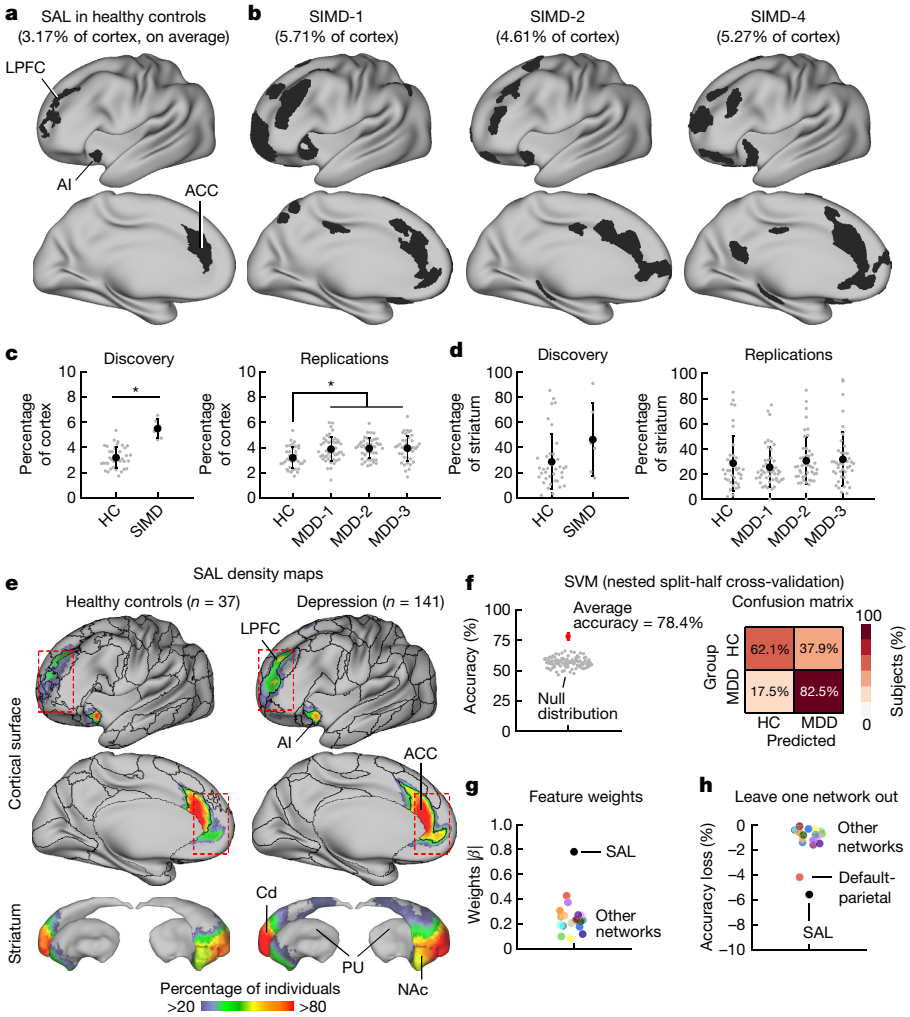

Fig. 1 | Frontostriatal salience network is expanded nearly twofold in the cortex of highly sampled individuals with depression. a, The salience network (black) has representation in LPFC, ACC and AI. **b**, The salience network in three representative individuals from the dataset referred to here as serial imaging of major depression (SIMD). **c**, The salience network was 73% larger on average in the SIMD dataset (significance assessed using a permutation test, $^*P = 0.001$, Bonferroni correction, Z-score = 6.19). This effect was replicated thrice (two-tailed independent sample t-tests, $n = 48$ from Weill Cornell Medicine, MDD-1: $T = 3.54$, $^*P = 0.01$, Bonferroni correction, Cohen's $d = 0.72$; another sample of $n = 45$ from Weill Cornell Medicine, MDD-2: $T = 4.17$, $^*P = 0.002$, Bonferroni correction, Cohen's $d = 0.84$; $n = 42$ from Stanford University, MDD-3: $T = 3.68$, $^*P = 0.008$, Bonferroni correction, Cohen's $d = 0.77$). Data are presented as mean ± s.d. **d**, No significant group differences in salience network representation in the striatum were observed in either the discovery (two-tailed permutation test, $P = 0.07$, uncorrected) or replication datasets (two-tailed independent sample t-tests, all $P > 0.43$, uncorrected). Data are presented as mean ± s.d. **e**, Density maps confirm that spatial locations of salience network nodes were similar in healthy controls and individuals with depression but that network borders extended further outwards from their centroids in each cortical zone in depression (red boxes). **f**, An SVM classifier distinguished individuals with depression from healthy controls above chance (accuracy 78.4%, significance assessed using a permutation test, $P = 0.001$) using the size of each functional network as features. **g**, Linear predictor coefficients (β) associated with the trained model. **h**, Change in model accuracy after exclusion of each network. Both **g** and **h** indicate that salience network size was the most important feature. ACC, anterior cingulate; AI, anterior insular cortex; Cd, caudate; HC, healthy controls; LPFC, lateral prefrontal; NAc, nucleus accumbens; PU, putamen; SAL, salience network; SVM, support vector machine.

Accordingly, expansion of the salience network in cortex was accompanied by contraction of neighbouring functional systems in the SIMD sample (Extended Data Fig. 3). However, the specific patterns of contraction did not replicate in all datasets—a finding we return to in the following section. Otherwise, consistent and reproducible group differences in network size were specific to the salience network (no significant differences in the size of any other network after correcting for several comparisons).

To better understand whether this effect was also detectable in large, previously published samples involving conventional single-echo fMRI data, we identified the salience network in group-average functional connectivity data from two large datasets involving $n = 812$ (ref. 47) and $n = 120$ (ref. 45) healthy controls, respectively, and in a third dataset involving $n = 299$ individuals with treatment-resistant depression scanned in association with a neuromodulation intervention study[48]. The cortical representation of the salience network was more than 70% larger in the 299-subject depression sample compared to two healthy control samples (Extended Data Fig. 4). Furthermore, highly similar patterns of salience network topology and functional connectivity were produced in split-half analyses of each SIMD dataset (Extended Data Fig. 5), indicating that salience network expansion was a robust and reproducible feature of the brains of these highly sampled individuals.

Given the magnitude of the effect reported in Fig. 1c, we went on to test whether individuals with depression could be distinguished algorithmically from healthy controls using only the size of each functional network as predictive features. Thus, we trained a linear support vector

machine classifier to differentiate individuals with depression from healthy control individuals on the basis of the size of all 20 functional networks, pooling data from $n = 37$ healthy controls acquired from five different scanners and $n = 141$ individuals with depression acquired from two different scanners from two different manufacturers (that is, all the data in Fig. 1c). The Methods and Supplementary Fig. 6 give details about classifier training. Overall, support vector machine classifiers correctly differentiated depression cases from healthy controls with 78.4% accuracy (permutation test, $P = 0.001$; Fig. 1f), correctly identifying 82.5% of depression cases, for a positive predictive value of 89.5%. Feature importance was evaluated by examining the linear predictor coefficients and calculating the change in accuracy after exclusion (Fig. 1g,h). As expected, salience network size was the most distinguishing feature. Together, these analyses indicate that the salience network is markedly expanded in most individuals with depression, with large effect sizes that are reproducible in several samples involving different data acquisition and analysis procedures, and sufficient in magnitude to support individual classifications with high accuracy rates.

Three salience network expansion modes

Individual differences in functional brain organization occur in two forms: ectopic intrusions, in which isolated pieces of a functional network are observed in an atypical location, and border shifts, in which the boundary of a network expands (or contracts) and encroaches on its neighbours[15]. Border shifts are heritable[49] and associated with known mechanisms of cortical expansion controlled by genetic programs that refine boundaries between functional areas during development and with experience or in response to environmental influences[50]. Furthermore, macroscale networks in both humans and non-human primates are organized in a hierarchy associated with cortical gradients in gene expression and functional properties[51], with unimodal sensorimotor areas at the base and heteromodal association areas such as the default mode network at the apex[52]. Thus, as a step towards understanding the mechanisms that give rise to cortical expansion of the salience network in depression, we tested whether it was driven primarily by border shifts or ectopic intrusions and whether it tended to affect lower-level, unimodal sensorimotor networks or heteromodal association areas positioned higher in this hierarchy. To this end, we first generated a central tendency functional network map for the 37 healthy controls (Fig. 2a). Second, we identified parts of the salience network in each of the 141 individuals with depression that did not overlap with the salience network in the group-average map for healthy controls and classified them as either ectopic intrusions or border shifts (Fig. 2b,c). Next, we calculated an encroachment profile for each subject, by quantifying the degree of encroachment on every other functional network, defined as the relative contribution of each functional network to the total surface area of the encroaching portion of the salience network (Fig. 2c).

This analysis confirmed that salience network expansion was not randomly distributed—instead, it was due primarily to border shifts affecting three neighbouring higher-order functional systems, with three distinct encroachment profiles occurring in different individuals. Although salience network expansion involved both ectopic intrusions and border shifts, the latter were more common (Fig. 2d) and both tended to result in encroachment on the default, frontoparietal or cingulo-opercular networks (Fig. 2e), not unimodal sensorimotor networks. Comparison to 73 independent molecular, microstructural, electrophysiological, developmental and functional brain maps from neuromaps toolbox[53] showed that salience network expansion frequently occurred in brain regions with less intracortical myelin and thus greater capacity for synaptic plasticity[54] and for which individual differences in functional connectivity[55] and the concentration of particular neurotransmitter receptors (μ-opioid[56] and histamine H_3 receptors[57]) are most pronounced (Extended Data Fig. 6). Further comparisons to maps of FC test–retest reliability and temporal signal-to-noise confirmed that these brain regions were not more susceptible to noise than chance (Supplementary Fig. 7). It was also evident that the salience network tended to encroach on specific functional networks in different cortical zones (Fig. 2f). For example, in the lateral prefrontal cortex, the salience network expanded rostrally and tended to displace the frontoparietal network. By contrast, in the anterior cingulate and anterior insular cortex, the default mode and cingulo-opercular networks were disproportionately affected, respectively. Clustering individuals by their encroachment profiles showed three distinct modes (Fig. 2g), involving predominantly the default mode network, the frontoparietal network or a combination of the frontoparietal and cingulo-opercular networks. This heterogeneity may partly explain our observation that the salience network was consistently expanded in all three datasets but corresponding contractions of other functional networks were more variable.

The results above indicate that salience network expansion is driven primarily by encroachment on the frontoparietal, cingulo-opercular and default mode networks and suggest that cortical space at the boundary between networks may be allocated to different functional systems in individuals with depression. To test this, and to further validate our findings, we compared the strength of functional connectivity between encroaching nodes of the salience network (dark grey vertices in the left part of Fig. 2c) and the functional networks that typically occupy that space in healthy controls. This analysis was performed using split halves of each individual's resting-state fMRI dataset to assess the stability of the salience network assignment associated with the encroaching vertices relative to the runner-up assignments (most often either the default mode, frontoparietal or cingulo-opercular network). As expected, the functional connectivity of encroaching salience network nodes with the rest of the salience network was significantly stronger (mean $Z(r) = 0.26$) than with the displaced networks (all mean $Z(r) < 0.12$), consistent with weakened connectivity between encroaching nodes and the functional networks that typically occupy that space in healthy controls (Extended Data Fig. 7). Together, these results show that frontostriatal salience network expansion is driven primarily by network border shifts that affect three specific higher-order functional systems and spare others, with distinct modes of encroachment occurring in three subgroups of patients.

Salience network topology is trait-like

Major depressive disorder is a fundamentally episodic condition defined by discrete periods of low mood interposed between periods of euthymia[58,59]. We evaluated if changes in salience network topology accompany changes in the overall severity of depression symptoms that occur during mood-state transitions—an hypothesis that our longitudinal SIMD dataset was well-suited to test. However, and consistent with previous work describing functional network topography in healthy adults as very stable features affected very little by cognitive state or daily variation[17,20], we found that salience network topology was stable over time in individuals with and without depression (Fig. 3a). Furthermore, within-subject analyses showed no significant correlation between fluctuations in depression symptoms (HDRS6, a more sensitive measure of changes on shorter timescales) and changes in salience network size over time in any of the densely sampled individuals in our SIMD dataset (Fig. 3b). To address the same question, we asked whether salience network size changed after a rapid acting antidepressant treatment, leveraging samples of patients scanned before and after a conventional 6-week course of repetitive transcranial magnetic stimulation (rTMS; $n = 90$) or an accelerated, 1-week intensive course of rTMS ($n = 45$). There was no significant pre-to-post change in salience network size in either sample (Fig. 3d). In addition, neither the severity of symptoms during the current episode (Fig. 3e) nor the total number of depressive episodes individuals reported experiencing during their lifetime (Fig. 3f) explained individual differences in salience network size. Collectively, these findings indicate that salience network

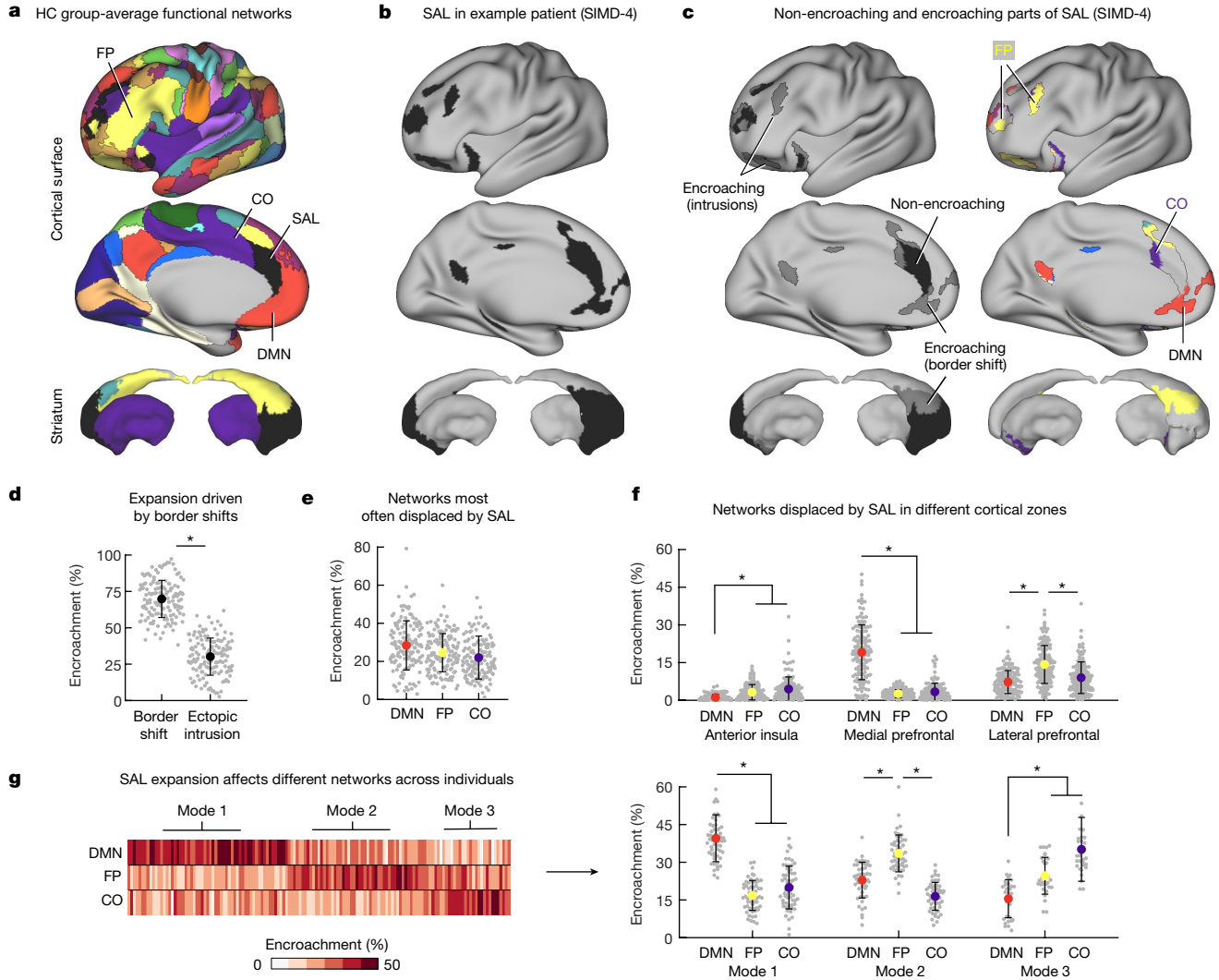

Fig. 2 | Three modes of salience network expansion in depression. a, Mode functional brain network assignments in cortex and striatum in HC. **b**, Salience network in a representative individual (SIMD-4) with depression. **c**, The parts of the salience network of each individual with depression that did and did not overlap with the HC are referred to as non-encroaching and encroaching, respectively. **d**, Salience network expansion more often due to shifts in network borders than ectopic intrusions—isolated patches of salience network in atypical locations (two-tailed paired sample *t*-test, $^*P < 0.001$, $n = 141$). Data are presented as mean ± s.d. **e**, The parietal subnetwork of the DMN (red), FP (yellow) and CO (purple) networks were most frequently displaced by salience network expansion. **f**, Salience network expansion affected different functional networks in different cortical zones. In the AI, the FP ($T = 5.94$, $^*P < 0.001$) and CO ($T = 6.42$, $^*P < 0.001$), networks were more affected than the default mode network. In the ACC, the DMN was more affected than either the FP ($T = 17.53$, $^*P < 0.001$) or CO/action-mode ($T = 15.25$, $^*P < 0.001$) networks. Finally, in LPFC, the FP was more affected than either the DMN ($T = 9.31$, $^*P < 0.001$) or CO ($T = 6.33$, $^*P < 0.001$). Statistical significance was assessed using two-tailed two-sample *t*-tests; all *P* values are Bonferroni corrected, $n = 141$. Data are presented as mean ± s.d. **g**, Individuals with depression clustered using their encroachment profiles (the relative contribution of each functional network to the total surface area of the encroaching portion of their salience network) revealed three distinct modes of encroachment across individuals. CO, cingulo-opercular; DMN, default mode; FP, frontoparietal.

expansion is a stable feature of individuals with major depressive disorder but not a marker of depressive episodes and unrelated to the severity of their symptom severity or to the chronicity of their illness.

These observations led us to propose that instead of driving changes in depressive symptoms over time, salience network expansion may be a stable marker of risk for developing depression. To test this hypothesis, we asked whether salience network expansion was present earlier in life, before the onset of depressive symptoms in individuals. Using data from the adolescent brain cognitive development (ABCD) study[60], we identified $n = 57$ children who did not have significant depressive symptoms when they were scanned at ages 10 and 12 years but then went on to develop clinically significant depressive symptoms at either age 13 or 14 years (Fig. 3g). An equal number of children from the ABCD study with no depressive symptoms at any time point were also identified as a control sample. Precision functional mapping showed that, on average, the salience network occupied 35.93% more of cortex in children with no current or previous symptoms of depression at the time of their fMRI scans but who subsequently developed clinically significant symptoms of depression, relative to children with no depressive symptoms at any study time point (Fig. 3g, 3.81% ± 1.58% of cortex in ABCD-MDD versus 2.80% ± 1.48% of cortex in ABCD-HC). There was no significant change in salience network size in the 2 years between the baseline and 2-year follow-up visits in either sample (Supplementary Fig. 8). A similar effect was observed in adults with late-onset depression (Extended Data Fig. 8). Together, these results show that cortical expansion of the salience network is a trait-like feature of brain network organization that is stable over weeks, months and years, unaffected by mood state and detectable in children before the onset of depression symptoms in adolescence.

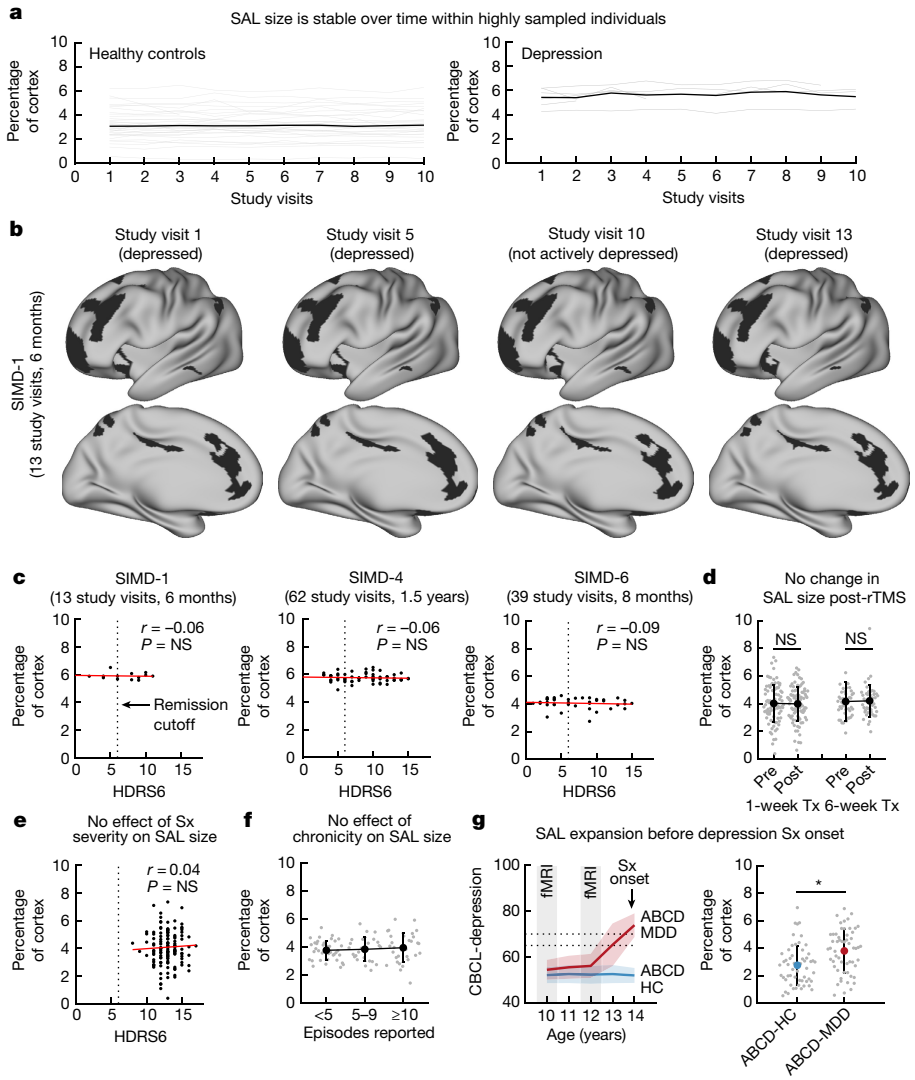

Fig. 3 | Salience network expansion is stable over time and present before symptom onset. a, Cortical representation of the salience network was stable in repeatedly scanned healthy controls (left) and individuals with depression (right). The first ten study visits for each individual are shown for visualization purposes. **b**, Salience network in a representative individual with depression that was scanned longitudinally to sample different mood states. **c**, No significant correlation between the severity of depressive symptoms (HDRS6) and salience network size in any repeatedly sampled individual with depression from the SIMD sample (Pearson correlation, all $P > 0.63$, two-tail test). **d**, No significant change in salience network size after a course of either a traditional 6-week (two-tailed paired sample *t*-test, $T = 0.58$, $P = 0.55$, uncorrected, $n = 90$) or accelerated 1-week (two-tailed paired sample *t*-test, $T = 0.58$, $P = 0.56$, uncorrected, $n = 45$) course of repetitive transcranial magnetic stimulation (rTMS). Data are plotted as mean ± s.d. **e**, Individual differences in salience network size were not significantly correlated with depression severity (HDRS6, Pearson correlation, $r = 0.04$, $P = 0.63$, uncorrected, two-tailed test). **f**, The number of depressive episodes experienced (inferred from the Mini-International Neuropsychiatric Interview) in each individual's lifetime in relation to the size of their salience network. Data are plotted as mean ± s.d. **g**, Children from the ABCD study scanned before the onset of elevated depression symptoms were identified (ABCD-MDD). Depression symptoms were operationalized using the DSM-oriented scale for depression from the CBCL (*T*-scores ≥70 are in the clinical range). The salience network was significantly larger in children who later developed clinically elevated symptoms of depression compared to children who did not (two-tailed independent sample *t*-test, $T = 3.50$, $^*P < 0.001$, Cohen's $d = 0.62$, $n = 114$). Data are plotted as mean ± s.d. NS, not significant; Sx, symptom; Tx, treatment.

Connectivity state predicts anhedonia

The results above indicate that topological features of the salience network, such as its size, shape and spatial location are stable over time and do not fluctuate with mood state. However, this observation does not preclude the possibility that functional connectivity between specific salience network nodes fluctuate in strength and that such fluctuations contribute to the emergence of depressive episodes and their subsequent remission. To test this, we first asked whether changes in functional connectivity strength between nodes of the salience network either co-occur with or predict fluctuations in symptom severity over time in individuals, focusing initially on hedonic function, a core feature of depression that is associated with frontostriatal circuits[61–66] and is aligned with the putative role of salience network[40,41,46] and accumbens–anterior cingulate circuits more specifically[67–69], in reward processing and goal-oriented effortful behaviour[61,70–72]. Our analyses focused on two of the patients from the SIMD dataset (SIMD-4 and SIMD-6) who were repeatedly scanned and assessed by clinicians longitudinally over 8–18 months, providing sufficient data for this analysis. This afforded an opportunity to ask for the first time at the level of single densely sampled individuals—whose data effectively served as independent, well-powered *n*-of-1 experiments[14,73]—how variability in brain network functional connectivity relates to fluctuations in specific symptom domains.

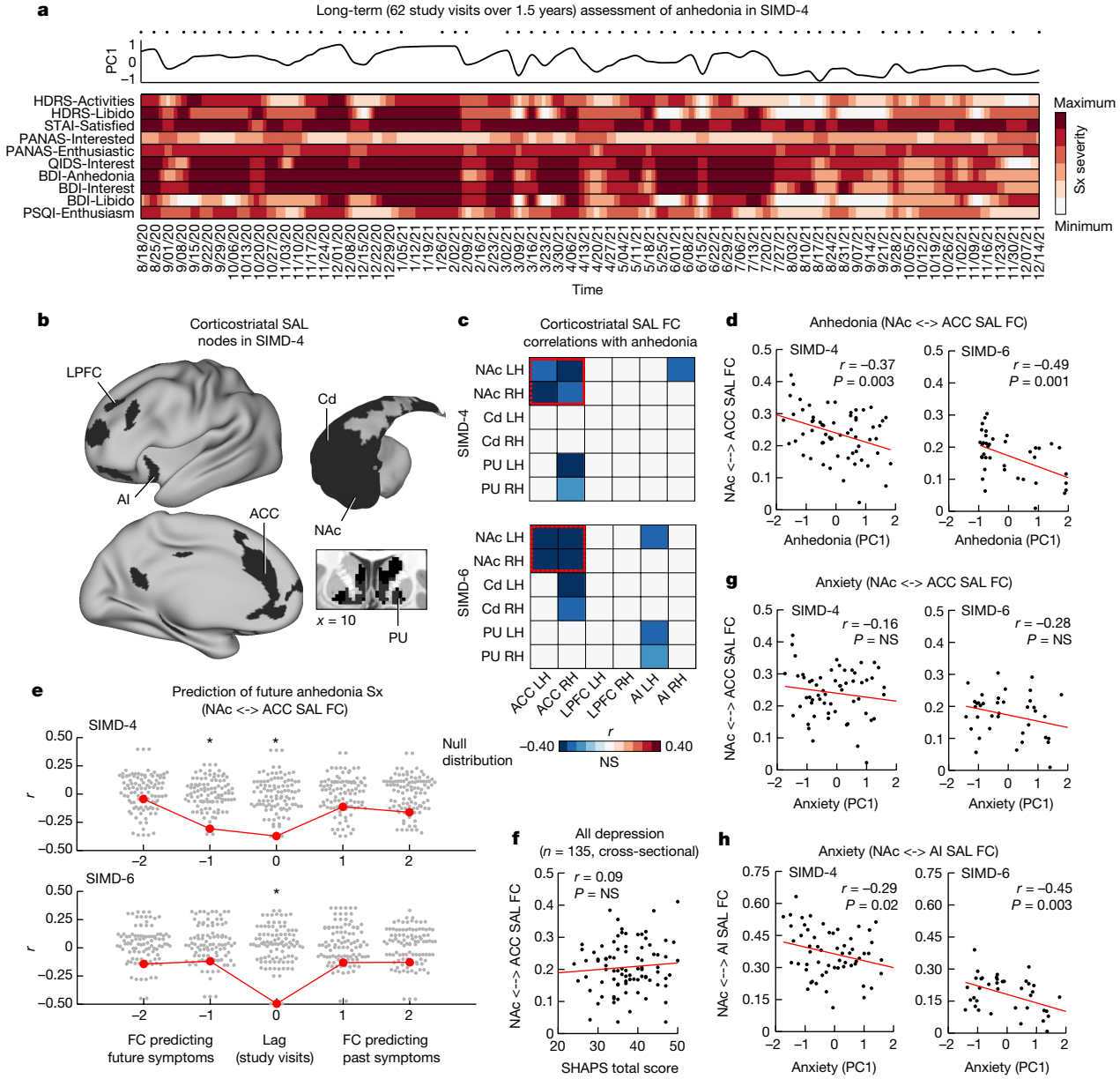

Fig. 4 | Frontostriatal salience network connectivity predicts fluctuations in anhedonia and anxiety symptoms in deeply sampled individuals with depression over time. a, Heat map summarizing fluctuations in individual items selected from a variety of clinical interviews and self-report scales related to anhedonia symptoms in a deeply sampled individual with depression (SIMD-4). Clinical data were resampled to days for visualization purposes (black dots mark the study visits). **b**, Frontostriatal nodes of the salience network in SIMD-4. **c**, Correlation matrices summarizing the association between FC strength between different cortico-striatal salience network nodes and fluctuations in the severity of anhedonia-related symptoms in both SIMD-4 and SIMD-6. **d**, FC between salience network nodes in the NAc and ACC most closely tracked fluctuations in the severity of anhedonia-related symptoms in both SIMD-4 (Pearson correlation, $r = -0.37$, $P = 0.003$) and SIMD-6 (Pearson correlation, $r = -0.49$, $P = 0.001$) across study visits. Statistical significance was assessed using two-tailed permutation tests with circular rotation to preserve temporal autocorrelation. **e**, Cross-correlation analyses indicated NAc ↔ ACC FC also predicted the severity of anhedonia-related symptoms at the following study visit in SIMD-4 (Pearson correlation, significance tested by means of permutation test, $r = -0.32$, $^*P = 0.004$) but not in SIMD-6. **f**, No significant correlation between individual differences in salience network NAc ↔ ACC FC strength and the severity of anhedonia-related symptoms across individuals (assessed using SHAPS, Pearson correlation, $r = 0.09$, $P = 0.41$). **g**, In SIMD-4 and SIMD-6, salience network NAc ↔ ACC FC was not significantly related to fluctuations in the severity of other depressive symptoms, such as anxiety. **h**, In contrast, FC between the NAc and AI was most closely related to fluctuations in the severity of anxiety-related symptoms (Pearson correlations, SIMD-4: $r = -0.29$, $P = 0.02$; SIMD-6: $r = -0.45$, $P = 0.004$, two-tailed tests), indicating different patterns of functional connectivity relate to different symptoms. FC, functional connectivity. AI, anterior insula; NAc, nucleus accumbens.

We began with SIMD-4 because this individual was studied over the longest period of time (62 study visits over 1.5 years) and had the most fMRI data (29.96 h of fMRI data in total) and reserved SIMD-6 as a replication dataset (57 study visits over 12 months, the initial 39 study visits had fMRI data before DBS implantation, 18.85 h of fMRI data in total). During a period spanning 1.5 years, we observed significant fluctuations in ten anhedonia-related measures (Fig. 4a), which were derived from five standardized depressive symptom scales and identified by a consensus clinical decision by three study co-authors (Supplementary Fig. 9), ranging from mild or negligible to severe. We tested whether changes in functional connectivity between nodes of the salience network were correlated with changes in anhedonia in this individual

over time, as measured by a principal component analysis of the ten anhedonia-related measures in Fig. 4a and summarized by the first component score. We found that functional connectivity between several cortical and striatal salience network nodes was correlated with changes in anhedonia over time (Fig. 4c,d), with the strongest effects observed for connectivity between the nucleus accumbens and anterior cingulate cortex. An identical analysis in SIMD-6, involving 39 study visits with clinical and fMRI data over 8 months, replicated this effect (Fig. 4c,d and Extended Data Fig. 9a,b). This finding remained significant in both individuals when including head motion at each study visit as a covariate.

Next, we asked whether salience network functional connectivity was predictive of symptom severity at future study visits and whether the effect was specific to anhedonia or extended to other symptom domains. Notably, a cross-correlation analysis examining correlations with symptoms in past, present and future study visits showed that functional connectivity between the salience network nodes in the nucleus accumbens and anterior cingulate was not only correlated with current anhedonia symptoms but also predicted the future emergence or remission of anhedonia symptoms in the next study visit in SIMD-4 (Fig. 4e, top), typically with a lag of approximately 1 week. The significance of this effect was confirmed using permutation tests with circular rotation to preserve temporal autocorrelation, indicating that accumbens–anterior cingulate connectivity at a given visit predicted future anhedonia approximately 1 week later, even after controlling for correlations in anhedonia measures over time. Of note, salience network connectivity correlations were replicated in SIMD-6 for current symptoms but not for future symptoms (Fig. 4e, bottom), which may relate to differences in their antidepressant treatments in this observational setting (SIMD-6 was undergoing maintenance electroconvulsive treatment unrelated to this study).

To determine whether changes in nucleus accumbens–anterior cingulate functional connectivity not only predicted changes in anhedonia in individual subjects over time but also explained individual differences in anhedonia at a given point in time, we repeated this analysis cross-sectionally using the entire $n = 135$ cohort of replication subjects using a standardized self-report measure of anhedonia. However, this analysis did not show a significant correlation between individual differences in functional connectivity between the anterior cingulate and nucleus accumbens and anhedonia across individuals (Fig. 4f), underscoring the value of within-subject analyses.

Finally, to evaluate the specificity of this effect, we asked whether nucleus accumbens–anterior cingulate connectivity was also associated with anxiety, a symptom domain that co-occurs with depression but is often dissociable from anhedonia (see Extended Data Fig. 10 for stacked anhedonia and anxiety symptom heatmaps). For example, 'dysphoric' (sadness and anhedonia) and 'anxiosomatic' (anxiety and somatic) symptoms were dissociable from one another in a recent study mapping response to rTMS intervention to different stimulation sites[74]. We did not observe a significant correlation between accumbens–anterior cingulate connectivity and anxiety in either individual (Fig. 4g), indicating a more important role for this circuit in anhedonia. Of note, there are several neuroimaging and circuit physiology studies implicating the insula in the expression of anxiety and the processing of aversive states[75–79]. Motivated by this work, we performed an analogous analysis asking whether changes in striatal connectivity with the anterior insula area of the salience network were correlated with fluctuations in anxiety symptoms over time in each subject. In accord with our prediction, we found that striatal connectivity with anterior insula was significantly correlated with anxiety symptoms in SIMD-4 and replicated this effect in SIMD-6 (Fig. 4h). An exploratory whole-brain analysis evaluating how salience network connectivity strength to the rest of the cortex relates to fluctuations in the severity of anhedonia and anxiety symptoms is summarized in Supplementary Fig. 10. Collectively, these findings show that, although the salience network is stably expanded in individuals with depression and that this expansion seems to occur early in life, frontostriatal connectivity in this network also fluctuates over time, and changes in striatal connectivity with the anterior cingulate and anterior insula track the emergence and remission of anhedonia and anxiety symptoms, respectively.

Interpreting differences in topology

In this work, precision functional mapping in deeply sampled individuals with depression showed a marked expansion of the salience network that was robust and reproducible in several samples, with medium to large effect sizes relative to previously reported neuroimaging abnormalities in depression. This effect was driven primarily by network border shifts that encroached on three specific functional systems—the frontoparietal, cingulo-opercular and default mode networks—with three distinct modes of encroachment in different individuals. This effect was stable over time, not sensitive to mood state or a marker of depressive episodes and emerged early in life in children who went on to develop depressive symptoms later in adolescence. At the same time, changes in striatal connectivity with anterior cingulate and anterior insula nodes of the salience network tracked the emergence and remission of anhedonia and anxiety, respectively, and predicted future changes in hedonic function in one individual. Of note, our analysis benefited from the use of precision functional mapping in combination with large quantities of high-quality, densely sampled multi-echo fMRI data, which may be critical for mapping individual differences in network topology precisely (Supplementary Fig. 12) and this might in part explain why these findings have not been reported in the literature previously.

Although more work will be required to elucidate the mechanisms underlying salience network expansion in depression, key results from this report and other studies point to at least two hypotheses. First, converging evidence from several sources indicates that individual differences in network topology are regulated by activity-dependent mechanisms and related to the extent to which a given network is actively used. So far, most studies evaluating variability in the size of functional areas or networks across individual humans or other animals have focused primarily on the motor and visual systems. These studies have shown how different body parts have distinct representations in the primary motor cortex (M1) that differ in size and cortical representation is closely related to the dexterity of the corresponding limb, such that the upper limbs occupy more cortical surface area than the lower limbs, as one example[80]. Motor training can increase the representation of the trained muscle or limb in M1 (refs. 81,82), whereas limb amputation, casting and congenital limb defects all decrease the representation of the disused limb and increase the representation of other body parts[83–85]. The total surface area of primary visual cortex (V1) can vary up to threefold in healthy young adults and is correlated with individual differences in visual awareness[86] and contrast sensitivity[87]. Likewise, total cortical representation of the frontoparietal network was found to be positively correlated with executive function abilities in children[88]. Together, these reports suggest that salience network expansion—accompanied by a corresponding contraction of the frontoparietal, cingulo-opercular or default mode networks—may reflect a reallocation of cortical territory and information processing priorities in individuals with depression, which could in turn contribute to alterations in salience network functions such as interoceptive awareness, reward learning, autonomic signal processing and effort valuation[30,40,41].

Second, converging data indicate that cortical network topology is strongly influenced not only by externally modulated, activity-dependent mechanisms but also by intrinsic genetic programs[50,89]. Numerous transcription factors regulate cell adhesion molecules, exhibit strong expression gradients across the cortical sheet during development and covary with aspects of cortical organization, including the size or location of functional areas[89,90]. Deletion of these patterning factors can result in contraction or expansion of functional areas[90]. Conversely, increased expression of Emx2 increases the size

of V1 and decreases the size of somatomotor areas[91,92]. Although our findings do not speak directly to this question, at least three observations are consistent with a role for intrinsic developmental genetic programs as opposed to exclusively activity-dependent mechanisms. First, salience network expansion was highly stable, irrespective of an individual's current mood state, indicating that acute mood-related changes in network activity did not influence network size. Second, salience network expansion emerged early in life, consistent with a developmentally regulated mechanism. And third, salience network expansion was driven by spatially organized border shifts, which are known to be heritable[19,93] and which tended to encroach on neighbouring networks in specific directions, expanding anteriorly and disproportionately targeting higher-order heteromodal association cortex although sparing unimodal sensorimotor areas.

Trait versus state effects in depression

Our findings may also open new avenues to addressing two fundamental challenges to using insights from clinical neuroimaging research to rethink our approach to diagnosing and treating depression. First, as noted above, MRI studies spanning two decades have identified anatomical and functional connectivity alterations that are robust and reproducible in large-scale meta-analyses but are highly variable across subjects with modest effect sizes (typically Cohen's $d = 0.10–0.35$), which complicates effects to leverage these effects for clinical purposes. By contrast, salience network expansion was observed in most individuals with depression in our sample, readily apparent on visual inspection and associated with medium to large effect sizes (Cohen's $d = 0.77–1.99$). This effect was detected without corrections for site- or scanner-induced biases—which can be a significant confound for multisite neuroimaging data.

Biomarkers in several areas of medicine come in different forms, some of which are sensitive to current symptoms, whereas others are stable trait-like markers of disease or a marker of risk for developing symptoms. Our study was not designed to comprehensively validate a neuroimaging biomarker for depression and future work will be needed to assess the specificity of our findings with respect to other forms of psychopathology or evaluate its potential clinical utility. A preliminary analysis indicated that the salience network is also larger than normal in two individuals with bipolar II disorder but not autism spectrum disorder or obsessive compulsive disorder (Supplementary Fig. 11), which might reflect common deficits in behavioural domains, such as reward processing[94], that are also linked to salience network function. However, our results do indicate that salience network expansion has the potential to help predict susceptibility to depression symptoms and could have important implications for designing therapeutic neuromodulation interventions, which could have widely varying effects due to individual differences in network topology[95,96]. Another caveat to keep in mind is that precise and reliable mapping of the salience network and consistent detection of salience network expansion in individuals with depression may require 1.5–2 h of high-quality fMRI data per subject (Supplementary Fig. 12), which may be an obstacle for retrospective analysis of traditional fMRI datasets not optimized for precision functional mapping at the individual level. It is also noteworthy that the brain network that we and others[3,41,45,46] have referred to as the salience network is sometimes called other names (Control C in ref. 97) or combined with the parietal memory network[98], whereas the brain network we refer to as cingulo-opercular/action-mode network[41] is sometimes called the salience/ventral attention network[97] (Supplementary Fig. 13). Developing a standardized functional brain network nomenclature[99] will improve the interpretability of insights gleaned from precision functional mapping such as in the present study.

Finally, our study provides proof-of-principle data to support the use of precision functional mapping and deep, longitudinal sampling for understanding cause and effect in clinical neuroimaging studies of depression. Our analyses show stable, trait-like differences in salience network topology that are not only associated with depression but also emerge early in life in children with no history of depression and predict the subsequent emergence of depressive symptoms in adolescence. At the same time, they show how changes in functional connectivity strength between specific salience network nodes track the emergence and remission of dysfunction in specific symptom domains in individuals over time and, in at least one individual, predict the future emergence of anhedonia symptoms at least 1 week before they occur. In this way, they show how dense sampling and longitudinal designs will open new avenues for understanding cause and effect and for designing personalized, prophylactic treatments.

Online content

Any methods, additional references, Nature Portfolio reporting summaries, source data, extended data, supplementary information, acknowledgements, peer review information; details of author contributions and competing interests; and statements of data and code availability are available at https://doi.org/10.1038/s41586-024-07805-2.

1. Winter, N. R. et al. Quantifying deviations of brain structure and function in major depressive disorder across neuroimaging modalities. *JAMA Psychiatry* **79**, 879–888 (2022).
2. Laumann, T. O. et al. Functional system and areal organization of a highly sampled individual human brain. *Neuron* **87**, 657–670 (2015).
3. Gordon, E. M. et al. Precision functional mapping of individual human brains. *Neuron* **95**, 791–807 (2017).
4. Braga, R. M. & Buckner, R. L. Parallel interdigitated distributed networks within the individual estimated by intrinsic functional connectivity. *Neuron* **95**, 457–471 (2017).
5. Duman, R. S. & Aghajanian, G. K. Synaptic dysfunction in depression: potential therapeutic targets. *Science* **338**, 68–72 (2012).
6. Duman, R. S., Aghajanian, G. K., Sanacora, G. & Krystal, J. H. Synaptic plasticity and depression: new insights from stress and rapid-acting antidepressants. *Nat. Med.* **22**, 238–249 (2016).
7. Lui, S. et al. Resting-state functional connectivity in treatment-resistant depression. *Am. J. Psychiatry* **168**, 642–648 (2011).
8. Williams, L. M. Precision psychiatry: a neural circuit taxonomy for depression and anxiety. *Lancet Psychiatry* **3**, 472–480 (2016).
9. Drysdale, A. T. et al. Resting-state connectivity biomarkers define neurophysiological subtypes of depression. *Nat. Med.* **23**, 28–38 (2017).
10. Murray, C. J. L. et al. Disability-adjusted life years (DALYs) for 291 diseases and injuries in 21 regions, 1990–2010: a systematic analysis for the Global Burden of Disease Study 2010. *Lancet* **380**, 2197–2223 (2012).
11. Wang, D. et al. Parcellating cortical functional networks in individuals. *Nat. Neurosci.* **18**, 1853–1860 (2015).
12. Poldrack, R. A. et al. Long-term neural and physiological phenotyping of a single human. *Nat. Commun.* **6**, 8885 (2015).
13. Fedorenko, E. The early origins and the growing popularity of the individual-subject analytic approach in human neuroscience. *Curr. Opin. Behav. Sci.* **40**, 105–112 (2021).
14. Naselaris, T., Allen, E. & Kay, K. Extensive sampling for complete models of individual brains. *Curr. Opin. Behav. Sci.* **40**, 45–51 (2021).
15. Seitzman, B. A. et al. Trait-like variants in human functional brain networks. *Proc. Natl Acad. Sci. USA* **116**, 22851–22861 (2019).
16. Kraus, B. T. et al. Network variants are similar between task and rest states. *Neuroimage* **229**, 117743 (2021).
17. Gratton, C. et al. Functional brain networks are dominated by stable group and individual factors, not cognitive or daily variation. *Neuron* **98**, 439–452 (2018).
18. Lynch, C. J. et al. Rapid precision functional mapping of individuals using Multi-Echo fMRI. *Cell Rep.* **33**, 108540 (2020).
19. Dworetsky, A. et al. Two common and distinct forms of variation in human functional brain networks. *Nat. Neurosci.* **27**, 1187–1198 (2024).
20. Anderson, K. M. et al. Heritability of individualized cortical network topography. *Proc. Natl Acad. Sci. USA* **118**, e2016271118 (2021).
21. Parsons, S. & McCormick, E. M. Limitations of two time point data for understanding individual differences in longitudinal modeling—what can difference reveal about change? *Dev. Cogn. Neurosci.* **66**, 101353 (2024).
22. Kraus, B. et al. Insights from personalized models of brain and behavior for identifying biomarkers in psychiatry. *Neurosci. Biobehav. Rev.* **152**, 105259 (2023).
23. Sendi, M. S. E. et al. Intraoperative neural signals predict rapid antidepressant effects of deep brain stimulation. *Transl. Psychiatry* **11**, 551 (2021).
24. Laumann, T. O. et al. Brain network reorganisation in an adolescent after bilateral perinatal strokes. *Lancet Neurol.* **20**, 255–256 (2021).
25. Dohm, K., Redlich, R., Zwitserlood, P. & Dannlowski, U. Trajectories of major depression disorders: a systematic review of longitudinal neuroimaging findings. *Aust. NZ J. Psychiatry* **51**, 441–454 (2017).
26. Brady, R. O. et al. Bipolar mood state reflected in cortico-amygdala resting state connectivity: a cohort and longitudinal study. *J. Affect. Disord.* **217**, 205–209 (2017).
27. Rey, G. et al. Dynamics of amygdala connectivity in bipolar disorders: a longitudinal study across mood states. *Neuropsychopharmacology* **46**, 1693–1701 (2021).

28. Scangos, K. W. et al. Closed-loop neuromodulation in an individual with treatment-resistant depression. *Nat. Med.* **27**, 1696–1700 (2021).
29. Alagapan, S. et al. Cingulate dynamics track depression recovery with deep brain stimulation. *Nature* **622**, 130–138 (2023).
30. Seeley, W. W. et al. Dissociable intrinsic connectivity networks for salience processing and executive control. *J. Neurosci.* **27**, 2349–2356 (2007).
31. Kundu, P. et al. Multi-echo fMRI: a review of applications in fMRI denoising and analysis of BOLD signals. *Neuroimage* **154**, 59–80 (2017).
32. Mayberg, H. S. et al. Reciprocal limbic-cortical function and negative mood: converging PET findings in depression and normal sadness. *Am. J. Psychiatry* **156**, 675–682 (1999).
33. Ressler, K. J. & Mayberg, H. S. Targeting abnormal neural circuits in mood and anxiety disorders: from the laboratory to the clinic. *Nat. Neurosci.* **10**, 1116–1124 (2007).
34. Goodkind, M. et al. Identification of a common neurobiological substrate for mental illness. *JAMA Psychiatry* **72**, 305–315 (2015).
35. Kaiser, R. H., Andrews-Hanna, J. R., Wager, T. D. & Pizzagalli, D. A. Large-scale network dysfunction in major depressive disorder: a meta-analysis of resting-state functional connectivity. *JAMA Psychiatry* **72**, 603–611 (2015).
36. Schmaal, L. et al. Cortical abnormalities in adults and adolescents with major depression based on brain scans from 20 cohorts worldwide in the ENIGMA Major Depressive Disorder Working Group. *Mol. Psychiatry* **22**, 900–909 (2017).
37. Mayberg, H. S. et al. Deep brain stimulation for treatment-resistant depression. *Neuron* **45**, 651–660 (2005).
38. Crowell, A. L. et al. Long-term outcomes of subcallosal cingulate deep brain stimulation for treatment-resistant depression. *Am. J. Psychiatry* **176**, 949–956 (2019).
39. Hamilton, M. A rating scale for depression. *J. Neurol. Neurosurg. Psychiatry* **23**, 56–62 (1960).
40. Seeley, W. W. The salience network: a neural system for perceiving and responding to homeostatic demands. *J. Neurosci.* **39**, 9878–9882 (2019).
41. Dosenbach, N. U. F., Raichle, M. E. & Gordon, E. M. The brain's cingulo-opercular action-mode network. Preprint at *PsyArXiv* https://doi.org/10.31234/osf.io/2vt79 (2024).
42. Kong, R. et al. Spatial topography of individual-specific cortical networks predicts human cognition, personality, and emotion. *Cereb. Cortex* **29**, 2533–2551 (2019).
43. Haber, S. N. & Knutson, B. The reward circuit: linking primate anatomy and human imaging. *Neuropsychopharmacology* **35**, 4–26 (2010).
44. Shepherd, G. M. G. Corticostriatal connectivity and its role in disease. *Nat. Rev. Neurosci.* **14**, 278–291 (2013).
45. Power, J. D. et al. Functional network organization of the human brain. *Neuron* **72**, 665–678 (2011).
46. Gordon, E. M. et al. Individualized functional subnetworks connect human striatum and frontal cortex. *Cereb. Cortex* **32**, 2868–2884 (2022).
47. Van Essen, D. C. et al. The WU-Minn Human Connectome Project: an overview. *Neuroimage* **80**, 62–79 (2013).
48. Blumberger, D. M. et al. Effectiveness of theta burst versus high-frequency repetitive transcranial magnetic stimulation in patients with depression (THREE-D): a randomised non-inferiority trial. *Lancet* **391**, 1683–1692 (2018).
49. Dworetsky, A. et al. Two common and distinct forms of variation in human functional brain networks. *Nat. Neurosci*. https://doi.org/10.1038/s41593-024-01618-2 (2024).
50. Krubitzer, L. A. & Seelke, A. M. H. Cortical evolution in mammals: the bane and beauty of phenotypic variability. *Proc. Natl Acad. Sci. USA* **109**, 10647–10654 (2012).
51. Wang, X.-J. Macroscopic gradients of synaptic excitation and inhibition in the neocortex. *Nat. Rev. Neurosci.* **21**, 169–178 (2020).
52. Margulies, D. S. et al. Situating the default-mode network along a principal gradient of macroscale cortical organization. *Proc. Natl Acad. Sci. USA* **113**, 12574–12579 (2016).
53. Markello, R. D. et al. neuromaps: structural and functional interpretation of brain maps. *Nat. Methods* **19**, 1472–1479 (2022).
54. Glasser, M. F., Goyal, M. S., Preuss, T. M., Raichle, M. E. & Van Essen, D. C. Trends and properties of human cerebral cortex: correlations with cortical myelin content. *Neuroimage* **93**, 165–175 (2014).
55. Mueller, S. et al. Individual variability in functional connectivity architecture of the human brain. *Neuron* **77**, 586–595 (2013).
56. Turtonen, O. et al. Adult attachment system links with brain mu opioid receptor availability in vivo. *Biol. Psychiat. Cogn. Neurosci. Neuroimaging* **6**, 360–369 (2021).
57. Gallezot, J.-D. et al. Kinetic modeling of the serotonin 5-HT(1B) receptor radioligand [(11)C] P943 in humans. *J. Cereb. Blood Flow Metab.* **30**, 196–210 (2010).
58. Post, R. M. et al. Morbidity in 258 bipolar outpatients followed for 1 year with daily prospective ratings on the NIMH life chart method. *J. Clin. Psychiatry* **64**, 680–690 (2003).
59. Malhi, G. S. & Mann, J. Depression. *Lancet* **392**, 2299–2312 https://doi.org/10.1016/s0140-6736(18)31948-2 (2018).
60. Casey, B. J. et al. The adolescent brain cognitive development (ABCD) study: imaging acquisition across 21 sites. *Dev. Cogn. Neurosci.* **32**, 43–54 (2018).
61. Kennerley, S. W., Walton, M. E., Behrens, T. E. J., Buckley, M. J. & Rushworth, M. F. S. Optimal decision making and the anterior cingulate cortex. *Nat. Neurosci.* **9**, 940–947 (2006).
62. Rushworth, M. F. S. & Behrens, T. E. J. Choice, uncertainty and value in prefrontal and cingulate cortex. *Nat. Neurosci.* **11**, 389–397 (2008).
63. Lim, B. K., Huang, K. W., Grueter, B. A., Rothwell, P. E. & Malenka, R. C. Anhedonia requires MC4R-mediated synaptic adaptations in nucleus accumbens. *Nature* **487**, 183–189 (2012).
64. Russo, S. J. & Nestler, E. J. The brain reward circuitry in mood disorders. *Nat. Rev. Neurosci.* **14**, 609–625 (2013).
65. Tye, K. M. et al. Dopamine neurons modulate neural encoding and expression of depression-related behaviour. *Nature* **493**, 537–541 (2013).
66. Pizzagalli, D. A. Depression, stress, and anhedonia: toward a synthesis and integrated model. *Annu. Rev. Clin. Psychol.* **10**, 393–423 (2014).
67. Lee, D., Seo, H. & Jung, M. W. Neural basis of reinforcement learning and decision making. *Annu. Rev. Neurosci.* **35**, 287–308 (2012).
68. Ruff, C. C. & Fehr, E. The neurobiology of rewards and values in social decision making. *Nat. Rev. Neurosci.* **15**, 549–562 (2014).
69. Fetcho, R. N. et al. A stress-sensitive frontostriatal circuit supporting effortful reward-seeking behavior. *Neuron* **112**, 473–487 (2024).
70. Hart, E. E., Stolyarova, A., Conoscenti, M. A., Minor, T. R. & Izquierdo, A. Rigid patterns of effortful choice behavior after acute stress in rats. *Stress* **20**, 19–28 (2017).
71. Quilodran, R., Rothé, M. & Procyk, E. Behavioral shifts and action valuation in the anterior cingulate cortex. *Neuron* **57**, 314–325 (2008).
72. Prévost, C., Pessiglione, M., Météreau, E., Cléry-Melin, M.-L. & Dreher, J.-C. Separate valuation subsystems for delay and effort decision costs. *J. Neurosci.* **30**, 14080–14090 (2010).
73. Newbold, D. J. & Dosenbach, N. U. F. Tracking plasticity of individual human brains. *Curr. Opin. Behav. Sci.* **40**, 161–168 (2021).
74. Siddiqi, S. H. et al. Distinct symptom-specific treatment targets for circuit-based neuromodulation. *Brain Stim.* **12**, e138 https://doi.org/10.1016/j.brs.2019.03.052 (2019).
75. Terasawa, Y., Shibata, M., Moriguchi, Y. & Umeda, S. Anterior insular cortex mediates bodily sensibility and social anxiety. *Soc. Cogn. Affect. Neurosci.* **8**, 259–266 (2013).
76. Gogolla, N. The insular cortex. *Curr. Biol.* **27**, R580–R586 (2017).
77. Deng, H. et al. A genetically defined insula-brainstem circuit selectively controls motivational vigor. *Cell* **184**, 6344–6360 (2021).
78. Nicolas, C. et al. Linking emotional valence and anxiety in a mouse insula–amygdala circuit. *Nat. Commun.* **14**, 5073 (2023).
79. Hsueh, B. et al. Cardiogenic control of affective behavioural state. *Nature* **615**, 292–299 (2023).
80. Penfield, W. & Boldrey, E. Somatic motor and sensory representation in the cerebral cortex of man as studied by electrical stimulation. *Brain* **60**, 389–443 (1937).
81. Karni, A. et al. Functional MRI evidence for adult motor cortex plasticity during motor skill learning. *Nature* **377**, 155–158 (1995).
82. Taubert, M., Mehnert, J., Pleger, B. & Villringer, A. Rapid and specific gray matter changes in M1 induced by balance training. *Neuroimage* **133**, 399–407 (2016).
83. Yu, X. J. et al. Somatotopic reorganization of hand representation in bilateral arm amputees with or without special foot movement skill. *Brain Res.* **1546**, 9–17 (2014).
84. Hahamy, A. et al. Representation of multiple body parts in the missing-hand territory of congenital one-handers. *Curr. Biol.* **27**, 1350–1355 (2017).
85. Nakagawa, K., Takemi, M., Nakanishi, T., Sasaki, A. & Nakazawa, K. Cortical reorganization of lower-limb motor representations in an elite archery athlete with congenital amputation of both arms. *Neuroimage Clin.* **25**, 102144 (2020).
86. Schwarzkopf, D. S., Song, C. & Rees, G. The surface area of human V1 predicts the subjective experience of object size. *Nat. Neurosci.* **14**, 28–30 (2011).
87. Himmelberg, M. M., Winawer, J. & Carrasco, M. Linking individual differences in human primary visual cortex to contrast sensitivity around the visual field. *Nat. Commun.* **13**, 3309 (2022).
88. Cui, Z. et al. Individual variation in functional topography of association networks in youth. *Neuron* **106**, 340–353 (2020).
89. Cadwell, C. R., Bhaduri, A., Mostajo-Radji, M. A., Keefe, M. G. & Nowakowski, T. J. Development and arealization of the cerebral cortex. *Neuron* **103**, 980–1004 (2019).
90. O'Leary, D. D. & Sahara, S. Genetic regulation of arealization of the neocortex. *Curr. Opin. Neurobiol.* **18**, 90–100 (2008).
91. Hamasaki, T., Leingärtner, A., Ringstedt, T. & O'Leary, D. D. M. EMX2 regulates sizes and positioning of the primary sensory and motor areas in neocortex by direct specification of cortical progenitors. *Neuron* **43**, 359–372 (2004).
92. Leingärtner, A. et al. Cortical area size dictates performance at modality-specific behaviors. *Proc. Natl Acad. Sci. USA* **104**, 4153–4158 (2007).
93. Alvarez, I. et al. Heritable functional architecture in human visual cortex. *Neuroimage* **239**, 118286 (2021).
94. Whitton, A. E., Treadway, M. T. & Pizzagalli, D. A. Reward processing dysfunction in major depression, bipolar disorder and schizophrenia. *Curr. Opin. Psychiatry* **28**, 7 (2015).
95. Lynch, C. J. et al. Automated optimization of TMS coil placement for personalized functional network engagement. *Neuron* https://doi.org/10.1016/j.neuron.2022.08.012 (2022).
96. Cash, R. F. H. & Zalesky, A. Personalized and circuit-based transcranial magnetic stimulation: evidence, controversies, and opportunities. *Biol. Psychiatry* https://doi.org/10.1016/j.biopsych.2023.11.013 (2023).
97. Yeo, B. T. T. et al. The organization of the human cerebral cortex estimated by intrinsic functional connectivity. *J. Neurophysiol.* **106**, 1125–1165 https://doi.org/10.1152/jn.00338.2011 (2011).
98. Kwon, Y. et al. Situating the parietal memory network in the context of multiple parallel distributed networks using high-resolution functional connectivity. Preprint at *bioRxiv* https://doi.org/10.1101/2023.08.16.553585 (2023).
99. Uddin, L. Q. et al. Controversies and progress on standardization of large-scale brain network nomenclature. *Netw. Neurosci* **7**, 864–905 (2023).

Methods

Datasets

The datasets used in this paper are described briefly below, with more demographic and clinical information provided in the Supplementary Information. No statistical tests were used to predetermine the sample sizes. Overall, the depression sample collectively consisted of 141 individuals (mean age 40.71 ± 13.82 years, 56.7% female) with a diagnosis of major depression (based on DSM-IV-TR criteria and confirmed by the Mini-International Neuropsychiatric Interview administered by a trained clinician) drawn from five sources—SIMD, mean age 29.47 ± 8.28 years, 3 female (F)/3 male (M), Weill Cornell rTMS 1 (conventional 6-week rTMS, mean age 40.89 ± 12.73 years, 27 F/21 M), Weill Cornell rTMS 2 (accelerated, 1-week rTMS, mean age 40.89 ± 12.73 years, 21 F/24 M), Stanford University rTMS (conventional 6-week rTMS, mean age 38.09 ± 12.77 years, 29 F/13 M) and Weill Cornell late-onset depression datasets (mean age 66.60 ± 5.31 years, 5 F/0 M). The healthy control sample collectively consisted of 37 healthy adults (mean age 31.72 ± 7.08 years, 11 F) drawn from six sources—the Weill Cornell multi-echo (mean age 33.42 ± 9.10 years, 0 F/7 M)[18,41], MyConnectome (a single 45-year-old male)[12], Midnight Scan Club (MSC; mean age 29.1 ± 3.3 years, 5 F/5 M)[3], cast-induced plasticity (a single 27-year-old male)[100], natural scenes dataset (NSD; mean age 26.50 ± 4.24 years, 6 F/2 M)[101] and Eskalibur datasets (mean age 31.4 ± 5.4 years, 5 F/5 M)[102]. We note that the MSC, MyConnectome and cast-induced plasticity study were obtained online (https://openneuro.org/) in a preprocessed, fully denoised and surface-registered format, and no further preprocessing or denoising was performed for the present study.

MRI acquisition

Serial imaging of major depression dataset. Data were acquired on a Siemens Magnetom Prisma 3 T scanner at the Citigroup Biomedical Imaging Center of Weill Cornell medical campus using a Siemens 32-channel head coil. Two multi-echo, multi-band resting-state fMRI scans were collected using a T2*-weighted echo-planar sequence covering the full brain (TR 1,355 ms; TE1 13.40 ms, TE2 31.11 ms, TE3 48.82 ms, TE4 66.53 ms and TE5 84.24 ms; FOV 216 mm; flip angle 68° (the Ernst angle for grey matter assuming a T1 value of 1,400 ms); 2.4 mm isotropic voxels; 72 slices; AP phase encoding direction; in-plane acceleration factor 2; and multi-band acceleration factor 6) with 640 volumes acquired per scan for a total acquisition time of 14 min and 27 s. Spin echo EPI images with opposite phase encoding directions (AP and PA) but identical geometrical parameters and echo spacing were acquired before each resting-state scan. Multi-echo T1-weighted (TR/TI 2,500/1,000 ms; TE1 1.7 ms, TE2 3.6 ms, TE3 5.5 ms and TE4 7.4 ms; FOV 256 mm; flip angle 8° and 208 sagittal slices with a 0.8 mm slice thickness) and T2-weighted anatomical images (TR 3,200 ms; TE 563 ms; FOV 256; flip angle 8° and 208 sagittal slices with a 0.8 mm slice thickness) were acquired at the end of each session.

Weill Cornell rTMS 1 and 2 datasets. MRI data were acquired on a Siemens Magnetom Prisma 3 T machine at the Citigroup Biomedical Imaging Center of Weill Cornell medical campus using a Siemens 32-channel head coil. Two multi-echo, multi-band resting-state fMRI scans were collected at each study visit using a T2*-weighted echo-planar sequence covering the full brain (TR 1,300 ms; TE1 12.60 ms, TE2 29.51 ms, TE3 46.42 ms and TE4 63.33 ms; FOV 216 mm; flip angle 67° (the Ernst angle for grey matter assuming a T1 value of 1,400 ms); 2.5 mm isotropic voxels; 60 slices; AP phase encoding direction; in-plane acceleration factor 2; and multi-band acceleration factor 4) with 650 volumes acquired per scan for a total acquisition time of 14 min and 5 s. Spin echo EPI images with opposite phase encoding directions (AP and PA) but identical geometrical parameters and echo spacing were acquired before each resting-state scan. Multi-echo T1-weighted (TR/TI 2,500/1,000 ms; TE1 1.7 ms, TE2 3.6 ms, TE3 5.5 ms and TE4 7.4 ms; FOV 256 mm; flip angle 8° and 208 sagittal slices with a 0.8 mm slice thickness) and T2-weighted anatomical images (TR 3,200 ms; TE 563 ms; FOV 256 mm; flip angle 8° and 208 sagittal slices with a 0.8 mm slice thickness) were acquired at the end of each session.

Stanford University rTMS dataset. MRI data were acquired on a GE SIGNA 3 T machine at the Center for Neurobiological Imaging on Stanford University campus using a Nova Medical 32-channel head coil. Four multi-echo, multi-band resting-state fMRI scans were collected using a T2*-weighted echo-planar sequence covering the full brain (TR 1,330 ms; TE1 13.7 ms, TE2, 31.60 ms, TE3 49.50 ms and TE4 67.40 ms; flip angle 67° (the Ernst angle for grey matter assuming a T1 value of 1,400 ms); 3 mm isotropic voxels; 52 slices; AP phase encoding direction; in-plane acceleration factor 2; and multi-band acceleration factor 4) with 338 volumes acquired per scan for a total acquisition time of 7 min and 30 s. Spin echo EPI images with opposite phase encoding directions (AP and PA) but identical geometrical parameters and echo spacing were acquired before each resting-state scan. T1-weighted and T2-weighted anatomical images were acquired at the end of each session.

Weill Cornell late-onset depression dataset. MRI data were acquired on a Siemens Magnetom Prisma 3 T machine at the Citigroup Biomedical Imaging Center of Weill Cornell medical campus using a Siemens 32-channel head coil. Two multi-echo, multi-band resting-state fMRI scans were collected at each study visit using a T2*-weighted echo-planar sequence covering the full brain (TR 1,300 ms; TE1 12.60 ms, TE2 29.51 ms, TE3 46.42 ms and TE4 63.33 ms; FOV 216 mm; flip angle 67° (the Ernst angle for grey matter assuming a T1 value of 1,400 ms); 2.5 mm isotropic voxels; 60 slices; AP phase encoding direction; in-plane acceleration factor 2; and multi-band acceleration factor 4) with 480 volumes acquired per scan for a total acquisition time of 10 min and 38 s. Spin echo EPI images with opposite phase encoding directions (AP and PA) but identical geometrical parameters and echo spacing were acquired before each resting-state scan. Multi-echo T1-weighted (TR/TI 2,500/1,000 ms; TE1 1.7 ms, TE2 3.6 ms, TE3 5.5 ms and TE4 7.4 ms; FOV 256 mm; flip angle 8° and 208 sagittal slices with a 0.8 mm slice thickness) and T2-weighted anatomical images (TR 3,200 ms; TE 563 ms; FOV 256 mm; flip angle 8° and 208 sagittal slices with a 0.8 mm slice thickness) were acquired at the end of each session.

Anatomical preprocessing and cortical surface generation

Anatomical data were preprocessed and cortical surfaces generated using the Human Connectome Project (HCP) PreFreeSurfer, FreeSurfer and PostFreeSurfer pipelines (v.4.3).

Multi-echo fMRI preprocessing

Preprocessing of multi-echo data minimized spatial interpolation and volumetric smoothing while preserving the alignment of echoes. The single-band reference (SBR) images (one per echo) for each scan were averaged. The resultant average SBR images were aligned, averaged, co-registered to the ACPC-aligned T1-weighted anatomical image and simultaneously corrected for spatial distortions using FSL topup and epi_reg programs. Freesurfer bbregister algorithm was used to refine this co-registration. For each scan, echoes were combined at each time point and a unique 6 DOF registration (one per volume) to the average SBR image was estimated using FSL MCFLIRT tool, using a four-stage (sinc) optimization. All of these steps (co-registration to the average SBR image, ACPC alignment and correcting for spatial distortions) were concatenated using FSL convertwarp tool and applied as a single spline warp to individual volumes of each echo after correcting for slice time differences using FSL slicetimer program. The functional images underwent a brain extraction using the co-registered brain extracted T1-weighted anatomical image as a mask and corrected for

signal intensity inhomogeneities using ANT N4BiasFieldCorrection tool. All denoising was performed on preprocessed, ACPC-aligned images.

Multi-echo fMRI denoising

Preprocessed multi-echo data were submitted to multi-echo ICA (ME-ICA[103]), which is designed to isolate spatially structured T2*-dependent (neurobiological; BOLD-like) and S0-dependent (non-neurobiological; not BOLD-like) signals and implemented using the tedana.py workflow[104]. In short, the preprocessed, ACPC-aligned echoes were first combined according to the average rate of T2* decay at each voxel across all time points by fitting the monoexponential decay, $S(t) = S0e^{-t/T2^*}$. From these T2* values, an optimally combined multi-echo (OC-ME) time series was obtained by combining echoes using a weighted average ($WTE = TE \times e^{-TE/T2^*}$). The covariance structure of all voxel time courses was used to identify main signals in the OC-ME time series using principal component and independent component analysis. Components were classified as either T2*-dependent (and retained) or S0-dependent (and discarded), primarily according to their decay properties across echoes. All component classifications were manually reviewed by C.J.L. and revised when necessary following the criteria described in ref. 105. Mean grey matter time-series regression was performed to remove spatially diffuse noise. Temporal masks were generated for censoring high-motion time points using a framewise displacement threshold of 0.3 mm and a backward difference of two TRs, for an effective sampling rate comparable to historical framewise displacement measurements (approximately 2–4 s). Before the framewise displacement calculation, head realignment parameters were filtered using a stopband Butterworth filter (0.2–0.35 Hz) to attenuate the influence of respiration[106] on motion parameters.

Single-echo fMRI denoising

The following denoising procedures were applied to the NSD and ABCD datasets. The NSD dataset was obtained in an already preprocessed (but not yet denoised) format. For the ABCD data, Fast Track (unprocessed) neuroimaging data were obtained by means of NDA command line utilities (https://github.com/NDAR/nda-tools) and subjected to the preprocessing steps used for multi-echo fMRI data (omitting steps involving combination of echoes). Preprocessed single-echo data were then submitted to ICA-AROMA. All component classifications were manually reviewed by C.J.L. and revised when necessary following the criteria described in ref. 105. Mean grey matter time-series regression was performed to remove spatially diffuse noise. Temporal masks were generated for censoring high-motion time points, as done for the multi-echo fMRI datasets.

Surface processing and CIFTI generation of fMRI data

The denoised fMRI time series was mapped to the individual's fsLR 32k midthickness surfaces with native cortical geometry preserved (using the -ribbon-constrained method), combined into the connectivity informatics technology initiative (CIFTI) format and spatially smoothed with geodesic (for surface data) and Euclidean (for volumetric data) Gaussian kernels ($\sigma = 2.55$ mm) using Connectome Workbench command line utilities[107]. This yielded time courses representative of the entire cortical surface, subcortex (accumbens, amygdala, caudate, hippocampus, pallidum, putamen, thalamus and brainstem) and cerebellum but excluding non-grey matter tissue. Spurious coupling between subcortical voxels and adjacent cortical tissue was mitigated by regressing the average time series of cortical tissue of less than 20 mm in Euclidean space from a subcortical voxel.

Precision mapping of functional brain networks in individuals

A functional connectivity matrix summarizing the correlation between the time courses of all cortical vertices and subcortical voxels across all study visits was constructed. Correlations between nodes 10 mm or less apart (geodesic and Euclidean space used for cortico–cortical and subcortical–cortical distance, respectively) were set to zero. Correlations between voxels belonging to subcortical structures were set to zero. Functional connectivity matrices were thresholded in such a way that they retained at least the strongest X% correlations (0.01%, 0.02%, 0.05%, 0.1%, 0.2%, 0.5%, 1%, 2% and 5%) to each vertex and voxel and were used as inputs for the InfoMap community detection algorithm[108], one of the most widely used approaches for delineating functional brain networks and their boundaries in individuals[2,3,12,18,41,45]. Free parameters (for example, the number of algorithm repetitions) for the Infomap algorithm were fixed across subjects. The total number of communities identified by Infomap is controlled in part by how many connections are retained in the functional connectivity matrix after thresholding. The optimal scale for further analysis across individuals was defined as the graph threshold producing the best size-weighted average homogeneity relative to the median of the size-weighted average homogeneity calculated from randomly rotated networks, as done in ref. 109. Size-weighted average homogeneity was maximized relative to randomly rotated communities at the 0.1% graph density and resulted in 89.13 ± 8.04 communities on average across individuals.

Each Infomap community was algorithmically assigned to one of 20 possible functional network identities (Default-Parietal, Default-Anterolateral, Default-Dorsolateral, Default-Retrosplenial, Visual-Lateral, Visual-Stream, Visual-V1, Visual-V5, Frontoparietal, Dorsal Attention, Premotor/Dorsal Attention II, Language, Salience, Cingulo-opercular/Action-mode[41], Parietal memory, Auditory, Somatomotor-Hand, Somatomotor-Face, Somatomotor-Foot, Auditory or Somato-Cognitive-Action) primarily according their functional connectivity and spatial locations relative to a specified set of priors. All algorithmic assignments were manually reviewed by C.J.L. and manually adjusted in the case of an ambiguous assignment. See Supplementary Fig. 14 for more details about algorithmic assignments and Supplementary Figs. 15 and 16 for the visualizations of the functional network priors used in this study.

Functional brain networks were also mapped brain-wide using the multiplex version of the InfoMap community detection algorithm[110]. In a multiplex network, physical nodes (brain regions) can exist in several layers (study visits). A temporal network (node × node × study visit) summarizing the correlation between the time courses of all cortical vertices and subcortical voxels across study visits was constructed for each patient. Correlations between nodes less than 10 mm apart (geodesic and Euclidean space used for cortico–cortical and subcortical–cortical distance, respectively) were set to zero. Correlations between voxels belonging to subcortical structures were set to zero. Links between layers were generated automatically using neighbourhood flow coupling. The temporal distance between layers was constrained to 1 using the --multilayer-relax-limit option to encode the temporal order of study visits. Multiplex functional network parcellations were used for the analyses performed in the section 'Salience network topology is trait-like' and Fig. 3a–e.

Calculating functional network size and spatial locations in individuals

We first measured the surface area (in mm^2) that each vertex in the individual's midthickness surface is responsible for (wb_command --surface-vertex-areas). Next, we calculated the relative contribution (size) of each functional network to the total cortical surface area by taking the total surface area of all network vertices in relation to the total cortical surface area. In the striatum, in which each voxel represents the same amount of tissue, the relative contribution of each functional network to the total striatal volume was calculated by taking the total number of network voxels in relation to the total striatal voxels. The statistical significances of group differences in network size were evaluated using permutation tests and independent sample t-tests (the latter implemented using Matlab ttest2.m function). Effect size

(Cohen's *d*) was calculated as the difference in group means divided by pooled standard deviation. Assumptions about equal variance were adjusted when appropriate (based on two-sample *F*-tests performed using Matlab vartest2.m function). The relative difference between groups was calculated as the absolute difference divided by network size in healthy controls. Density maps were created by calculating the percentage of individuals with salience network representation at each cortical vertex or striatum voxel. These procedures collectively correspond to the analyses performed in the section 'Connectivity state predicts anhedonia' and Fig. 1c–e.

Classification analysis

Functional network size (the percentage of total cortical surface area occupied by each network, 20 networks/features total) were used as predictive features in a support vector machine classifier to distinguish individuals with depression and healthy controls. The model was trained using repeated (100 iterations) nested split-half (twofold) cross-validation with a grid search optimization strategy for hyperparameter tuning (box constraint and kernel size). The synthetic minority oversampling technique (SMOTE[111]) was used to prevent classification bias in favour of the majority class and was performed on training data only to prevent data leakage. Classification accuracy was calculated as the percentage of correct predictions and statistical significance assessed using permutation tests (shuffled diagnostic labels and 1,000 iterations). A confusion matrix was created using Matlab confmat.m function. Feature importance was evaluated by iteratively omitting each functional network and evaluating the resulting loss in accuracy. These procedures collectively are related to the analyses performed in the section 'Salience network expansion in depression' and Fig. 1f–i.

Evaluating how salience network expansion displaces other functional systems

The parts of each depressed individual's salience network map that did and did not overlap with the salience network in the group-average healthy control map were operationalized as 'non-encroaching' and 'encroaching', respectively. The group-average healthy control map was obtained by calculating the mode assignment across healthy controls at each point in the brain. Encroaching clusters were identified (wb_command -cifti-find-clusters) and were classified as border shifts if any part of the cluster was within 3.5 mm (in geodesic space) of a salience network vertex in the group-average healthy control map, and as ectopic intrusions if they did not, as done in ref. 41. An encroachment profile was calculated as the relative contribution of each functional network to the total surface area of the encroaching portion of the salience network. Individuals were clustered on the basis of the similarity of their encroachment profiles using the Louvain method (community_louvain.m function from the Brain Connectivity Toolbox[112]). These procedures correspond to the analyses performed in the section 'Three salience network expansion modes' and Fig. 2a–g.

Assessing the stability of salience network topography across time

The multiplex versions of each individual's salience network were used to assess the extent to which network topography (size) varied across study time points in highly sampled individuals with and without depression. Variability in salience network size was correlated with the overall severity of depressive symptoms (HDRS6) using Matlab corr.m function. In the replication samples (Weill Cornell Medicine rTMS 1, Weill Cornell Medicine rTMS 2 and Stanford University rTMS samples), we assessed pre-to-post change in salience network topography using paired two-tailed paired sample *t*-tests by means of Matlab ttest.m function. Data were binned according to treatment duration (conventional 6-week rTMS or accelerated 1-week rTMS). The number of depressive episodes in each individual's lifetime was inferred from their Mini-International Neuropsychiatric Interview. These procedures collectively correspond to the analyses performed in the section 'Salience network topology is trait-like' and Fig. 3.

Evaluating salience network topography early in life before symptom onset

We used the ABCD dataset (release 5.0) to test if atypical salience network topology precedes the onset of depression symptoms. Symptoms of depression in the ABCD study were operationalized using the ASEBA DSM-oriented scale for depression (mh_p_cbcl.csv) from the ABCD parent child behaviour checklist (CBCL). After excluding subjects with missing behavioural data or those with MRI data flagged internally ABCD for data quality issues, we identified $n = 58$ subjects (37 F) meeting criteria for onset of clinical depression symptoms at the 3-year follow-up (*t*-score 70 or more at or after the 3-year follow-up and *t*-scores below 65 at the previous study visits). One participant's data were not accessible on Fast Track, resulting in $n = 57$ total. An equal number of subjects with no clinically significant depression symptoms at any study time point (*t*-scores more than 65 at all study time points) were randomly selected as a control sample. The statistical significance of group differences in salience network size were evaluated using permutation tests and independent sample *t*-tests (the latter implemented using Matlab ttest2.m function). Assumptions about equal variance were adjusted when appropriate (based on two-sample *F*-tests performed using Matlab vartest2.m function). These procedures collectively correspond to the analyses performed in the section 'Salience network topology is trait-like' and Fig. 3g.

Longitudinal analyses relating changes in connectivity with symptom severity

Composite measures of anhedonia- and anxiety-related symptoms were obtained instructing three clinicians (I.E., J.D.P. and N.S.) to quantify (on a scale of 0–3; 0, not at all; 1, somewhat; 2, largely; 3, very strongly) the extent to each item from the battery of clinical scales administered to the SIMD subjects reflects anhedonia- or anxiety-related symptoms. Items assigned a score of 1 or greater by all three clinicians were included in the composite measures (Supplementary Fig. 9). For each subject, separately, the consensus items were mininum–maximum normalized, adjusted for valence (so that higher scores reflect more severe symptoms across all items) and then subjected to a principal component analysis to extract a time course (PC1) of anhedonia or anxiety severity across study visits. To validate this approach, we quantified the similarity to validated measures of anhedonia and anxiety using independent data and observed good correspondence (Pearson correlations more than 0.4). Functional connectivity strength between all pairs of cortical (anterior cingulate, lateral prefrontal and anterior insula cortex) and striatal (nucleus accumbens, caudate and putamen) nodes of the salience network was calculated for each study visit, separately, and correlated with the anhedonia or anxiety PC1. This analysis was constrained to the three major cortical and striatal nodes of the salience network in part to reduce the likelihood of false positives. Correlations not exceeding chance (based on null distribution of correlation coefficients obtained using rotated clinical data) were set to zero. Circular permutation tests (using Matlab circshift.m function) were used to preserve temporal autocorrelation. Cross-correlation analyses were performed using Matlab crosscorr.m function (with NumLags set to 2). For the cross-sectional analysis, the total Snaith–Hamilton pleasure scale (SHAPS[113]) score was calculated using baseline clinical data. These procedures collectively correspond to the analyses performed in the section 'Connectivity state predicts anhedonia' and Fig. 4.

Clinical trial information

A portion of the data used in this report was obtained from the biomarker-guided rTMS for treatment-resistant depression study (NCT04041479), randomized controlled trial of conventional versus

theta burst rTMS (HFL versus TBS) (NCT01887782) and accelerated TMS for depression and obsessive compulsive disorder studies (NCT04982757).

Reporting summary

Further information on research design is available in the Nature Portfolio Reporting Summary linked to this article.

Data availability

An example subject (HC-1) from the Weill Cornell Multi-echo dataset is available in an OpenNeuro repository at https://openneuro.org/datasets/ds005118/versions/1.0.0. Other data from the Weill Cornell Multi-echo and Eskalibur datasets are available on request from the corresponding authors of their respective publications, pending institutional approval of a data-sharing agreement in compliance with their respective IRB protocols. Data from the MyConnectome dataset are available on OpenNeuro repository at https://openneuro.org/datasets/ds000031/versions/2.0.2. Data from the MSC dataset are available in the OpenNeuro repository at https://openneuro.org/datasets/ds000224/versions/1.0.4. Data from the cast-induced plasticity dataset is available in the OpenNeuro repository at https://openneuro.org/datasets/ds002766/versions/3.0.0. Data from the natural scenes dataset are available from Amazon Web Services at https://registry.opendata.aws/nsd/. The ABCD data used in this report are from Annual Release (5.0). Data from individual subjects with depression are a part of ongoing clinical trials and not publicly available now but will be made available after completion of the trials through the NIMH Data Archive and other clinical data repositories.

Code availability

Code for preprocessing multi-echo fMRI data is maintained in an online repository (https://github.com/cjl2007/Liston-Laboratory-MultiEchofMRI-Pipeline). Code for performing the precision functional mapping and network size calculations described in this manuscript are maintained in an online repository (https://github.com/cjl2007/PFM-Depression). Software packages incorporated into the above pipelines for data analysis included: Matlab R2019a, https://www.mathworks.com/; Connectome Workbench 1.4.2, http://www.humanconnectome.org/software/connectome-workbench.html; Freesurfer v6, https://surfer.nmr.mgh.harvard.edu/; FSL 6.0, https://fsl.fmrib.ox.ac.uk/fsl/fslwiki; and Infomap, https://www.mapequation.org.

100. Newbold, D. J. et al. Plasticity and spontaneous activity pulses in disused human brain circuits. *Neuron* **107**, 580–589 (2020).
101. Allen, E. J. et al. A massive 7T fMRI dataset to bridge cognitive neuroscience and artificial intelligence. *Nat. Neurosci.* **25**, 116–126 (2022).
102. Moia, S. et al. ICA-based denoising strategies in breath-hold induced cerebrovascular reactivity mapping with multi echo BOLD fMRI. *Neuroimage* **233**, 117914 (2021).
103. Kundu, P. et al. Integrated strategy for improving functional connectivity mapping using multiecho fMRI. *Proc. Natl Acad. Sci. USA* **110**, 16187–16192 (2013).
104. DuPre, E. et al. TE-dependent analysis of multi-echo fMRI with tedana. *J. Open Source Softw.* **6**, 3669 (2021).
105. Griffanti, L. et al. Hand classification of fMRI ICA noise components. *Neuroimage* **154**, 188–205 (2017).
106. Power, J. D. et al. Distinctions among real and apparent respiratory motions in human fMRI data. *Neuroimage* **201**, 116041 (2019).
107. Marcus, D. S. et al. Human Connectome Project informatics: quality control, database services, and data visualization. *Neuroimage* **80**, 202–219 (2013).
108. Rosvall, M. & Bergstrom, C. T. Maps of random walks on complex networks reveal community structure. *Proc. Natl Acad. Sci. USA* **105**, 1118–1123 (2008).
109. Gordon, E. M. et al. Default-mode network streams for coupling to language and control systems. *Proc. Natl Acad. Sci. USA* **117**, 17308–17319 (2020).
110. De Domenico, M., Lancichinetti, A., Arenas, A. & Rosvall, M. Identifying modular flows on multilayer networks reveals highly overlapping organization in interconnected systems. *Phys. Rev. X* **5**, 011027 (2015).
111. Chawla, N. V., Bowyer, K. W., Hall, L. O. & Kegelmeyer, W. P. SMOTE: synthetic minority over-sampling technique. *J. Artif. Intell. Res.* **16**, 321–357 (2002).
112. Rubinov, M. & Sporns, O. Complex network measures of brain connectivity: uses and interpretations. *Neuroimage* **52**, 1059–1069 (2010).
113. Snaith, R. P. et al. A scale for the assessment of hedonic tone the Snaith–Hamilton pleasure scale. *Br. J. Psychiatry* **167**, 99–103 (1995).

Acknowledgements We thank the staff at the Citigroup Biomedical Imaging Center for assistance with data collection. We thank all study participants and especially the SIMD study participants for their time and dedication to science. R. Kong and T. Yeo helped with implementing the multi-session hierarchical Bayesian modelling[42] method. This work was supported by grants to C.L. from the National Institute of Mental Health, the National Institute on Drug Addiction, the Hope for Depression Research Foundation and the Foundation for OCD Research. C.J.L. was supported by an NIMH F32 National Research Service Award (F32MH120989). N.S. was supported by K23 MH123864. Work on 'Personalized therapeutic neuromodulation for anhedonic depression' is supported by Wellcome Leap as part of the Multi-Channel Psych Program. M.L. was supported by Deutsche Forschungsgemeinschaft (DFG grant CRC 1193, subproject B01).

Author contributions C.J.L., I.E., J.D.P. and C.L. conceived this work. Data acquisition, analysis and interpretation were conducted by C.J.L., I.E., T.N., A. Ayaz, S.Z., D.W., N.M., M.J., M.C., J.C., I.S., C.H., M.L., H.B., D.B., L.W.V., N.S., E.G., S.M., C.C.-G., J.D., F.V.-R., Z.J.D., D.M.B., K.K., A. Aloysi, E.M.G., M.T.B., N.W., J.D.P., B.Z., L.G., F.M.G. and C.L. Manuscript writing and revision was done by C.J.L., I.E., E.M.G., J.D.P. and C.L. Study authors C.J.L., I.E., M.L. and J.D.P. were included as participants.

Competing interests C.L. and C.J.L. are listed as inventors for Cornell University patent applications on neuroimaging biomarkers for depression which are pending or in preparation. C.L. has served as a scientific advisor or consultant to Compass Pathways PLC, Delix Therapeutics and Brainify.AI. The remaining authors declare no competing interests.

Additional information

Supplementary information The online version contains supplementary material available at https://doi.org/10.1038/s41586-024-07805-2.

Correspondence and requests for materials should be addressed to Charles J. Lynch or Conor Liston.

Peer review information *Nature* thanks Avram Holmes, Theodore Satterthwaite, Chao-Gan Yan and the other, anonymous, reviewer(s) for their contribution to the peer review of this work.

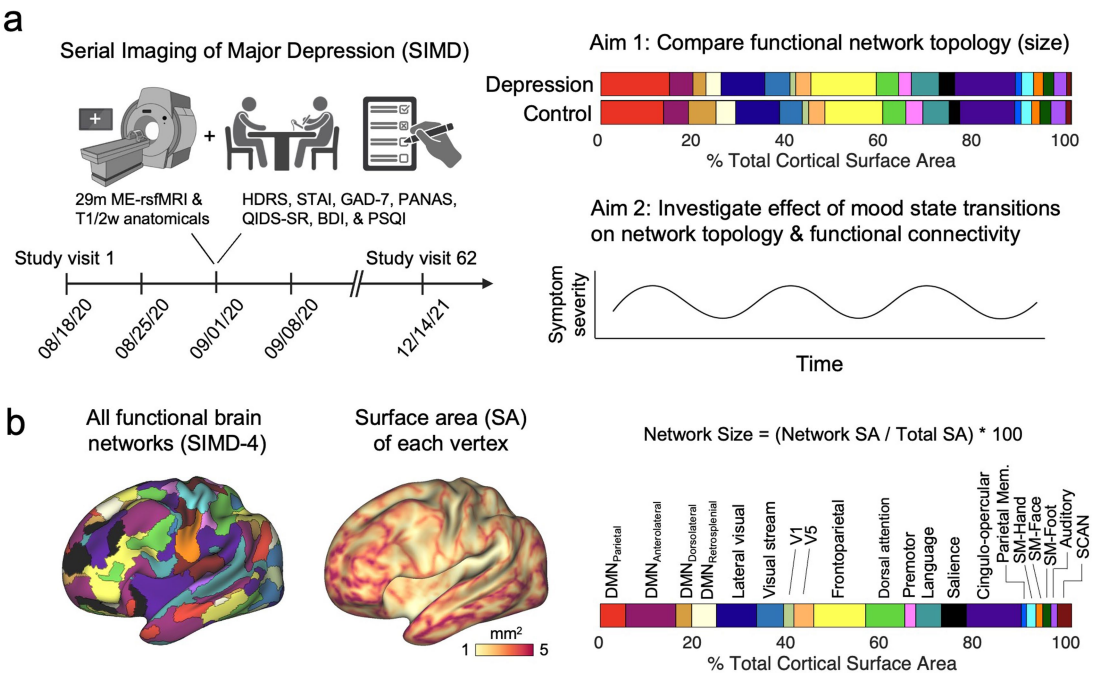

Extended Data Fig. 1 | Serial Imaging of Major Depression. a, The SIMD project involved repeated multi-echo resting-state fMRI scans (ME-rsfMRI) and clinical assessments of six individuals with depression over long periods of time. Precision functional mapping was then used to 1) investigate differences in functional network topology, specifically size relative to healthy controls, and 2) identify which atypical aspects of network topology or connectivity are stable versus sensitive to mood state within individuals as the severity of their symptoms fluctuated, and they cycled in and out of depressive episodes. Images created with BioRender.com. **b**, The relative contribution (size) of each functional network to the total cortical surface area was obtained by taking the total surface area of all network vertices in relation to the total cortical surface area. This approach controls for fact that each cortical vertex represents a different amount of surface area (SA). In the striatum, where each voxel represents the same amount of tissue, the relative contribution of each functional network to the total striatal volume was calculated by taking the total number of network voxels in relation to the total striatal voxels.

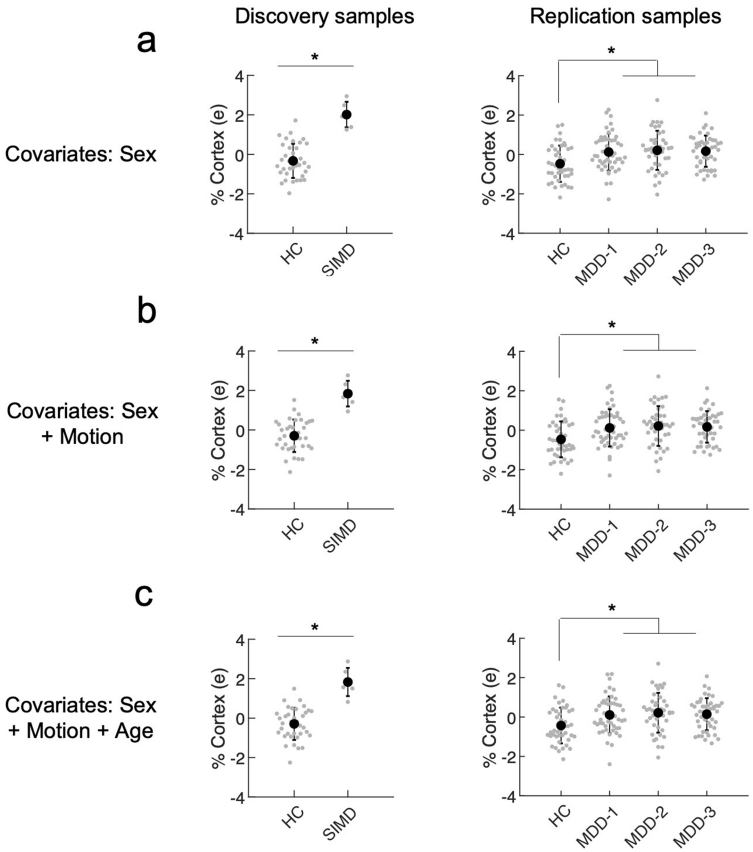

Extended Data Fig. 2 | Salience network expansion in depression remains statistically significant when controlling for sex ratio imbalance, and individual differences in head motion and age. a, Salience network size was regressed against sex (a variable of non-interest that differs between the two groups) and group comparisons were repeated using the residuals (*e*). The salience network was still significant larger in the Serial Imaging of Major Depression (SIMD; two-tailed independent sample t-test, $P < 0.001$, T = 7.02, and Cohen's $d = 2.09$) and in all three replication samples (two-tailed independent sample t-tests, all $P < 0.001$, T's > 3.00, and Cohen's $d > 0.6$) relative to healthy controls. **b-c**, This analysis was repeated when also including head motion (operationalized as the % of volume retained after motion censoring) and age (in years) as additional covariates. In all of these models, the salience network remained significantly larger in the SIMD (two-tailed, independent sample t-test, $P < 0.001$, $T = 6.75$, and Cohen's d = 2.06) and in all three replication samples (two-tailed independent sample t-tests, all P's ≤ 0.002, T's > 2.2, and Cohen's d > 0.56) relative to healthy controls. All error bars represent standard deviation.

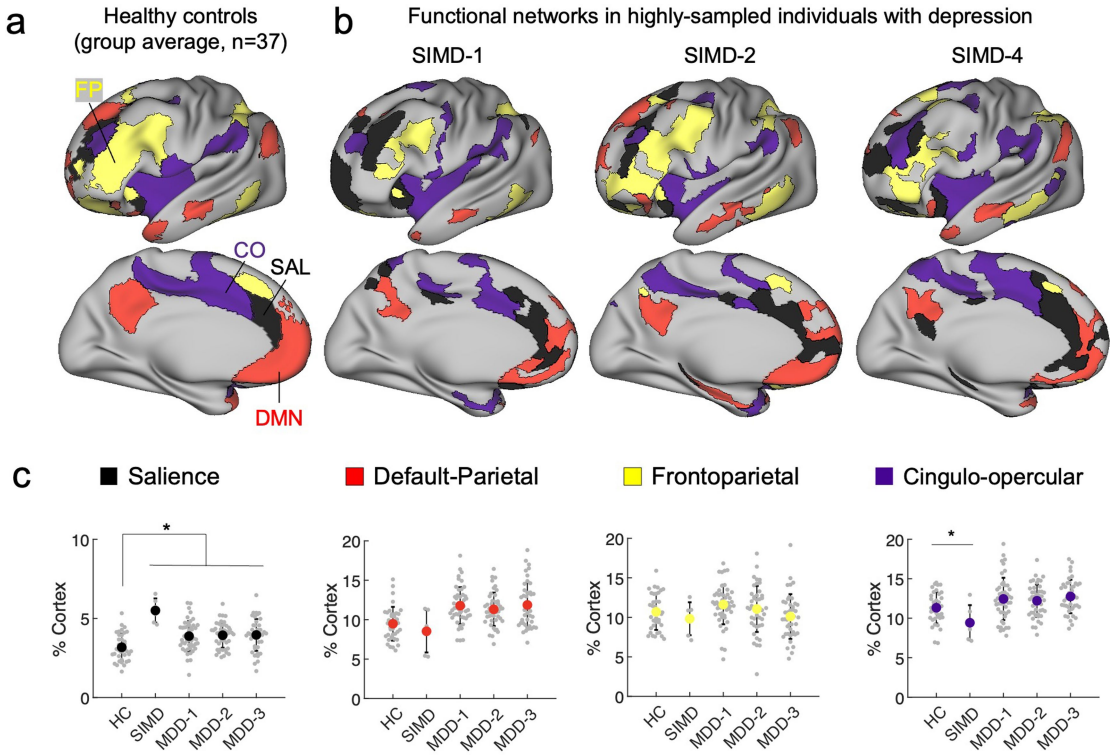

Extended Data Fig. 3 | Expansion of the salience network accompanied by contraction of neighboring functional systems. a-b, The salience (SAL, black), default mode (DMN, red), frontoparietal (FP, yellow), and cingulo-opercular (CO, purple) networks in a group-average map of healthy controls versus 3 representative individuals with depression. Expansion of the salience network in cortex (see Fig. 1c) was accompanied in some cases by contraction of other functional networks – most notably the cingulo-opercular network (two-tailed permutation test, $^*P = 0.04$, uncorrected, Z-score = 2.09, n = 43), but this effect was not observed in any of the replication samples. All error bars represent standard deviation.

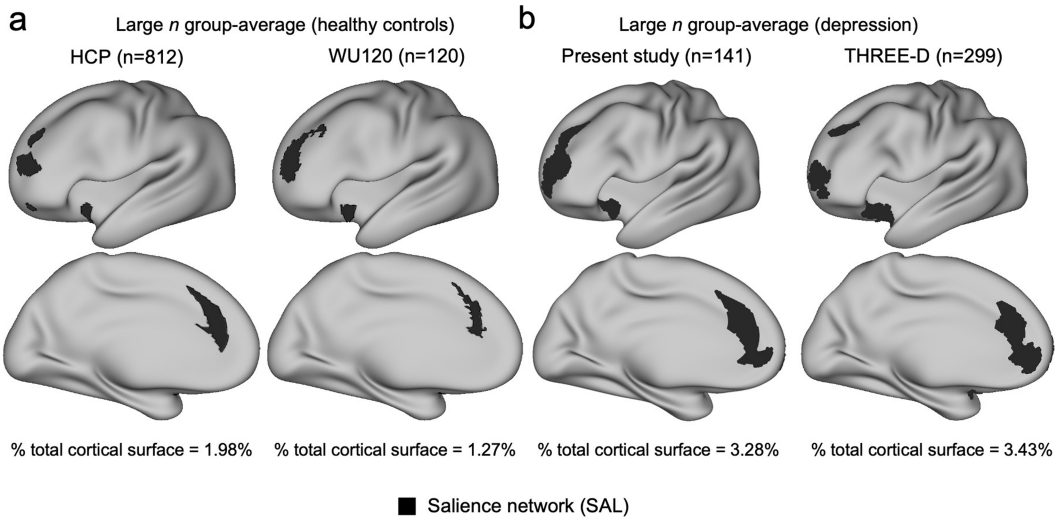

Extended Data Fig. 4 | Evidence of salience network expansion in large *n* group-average datasets. a, Salience network mapped using two large *n* group-average data from previous studies of healthy controls occupy 1.27% and 1.98% of cortex. The group-average HCP functional connectivity matrix (which only includes subjects with resting-state fMRI data reconstructed with the r227 recon algorithm) was obtained from the S1200 release and subjected to the same precision functional mapping procedures applied to individual subjects in the main text. The WU120 salience network map was obtained online (https://balsa.wustl.edu/jNXKl). **b**, Salience network mapped using large n group-average data and previous studies of depression occupies between 3.28% (mode assignment of all individuals with depression in current study) and 3.43% of total cortical surface area. Group-averaged functional connectivity was calculated in the THREE-D sample using group-level PCA (MELODIC Incremental Group-PCA, MIGP), and the resultant group-average FC matrix was subjected to the same precision functional mapping procedures applied to individual subjects in the main text.

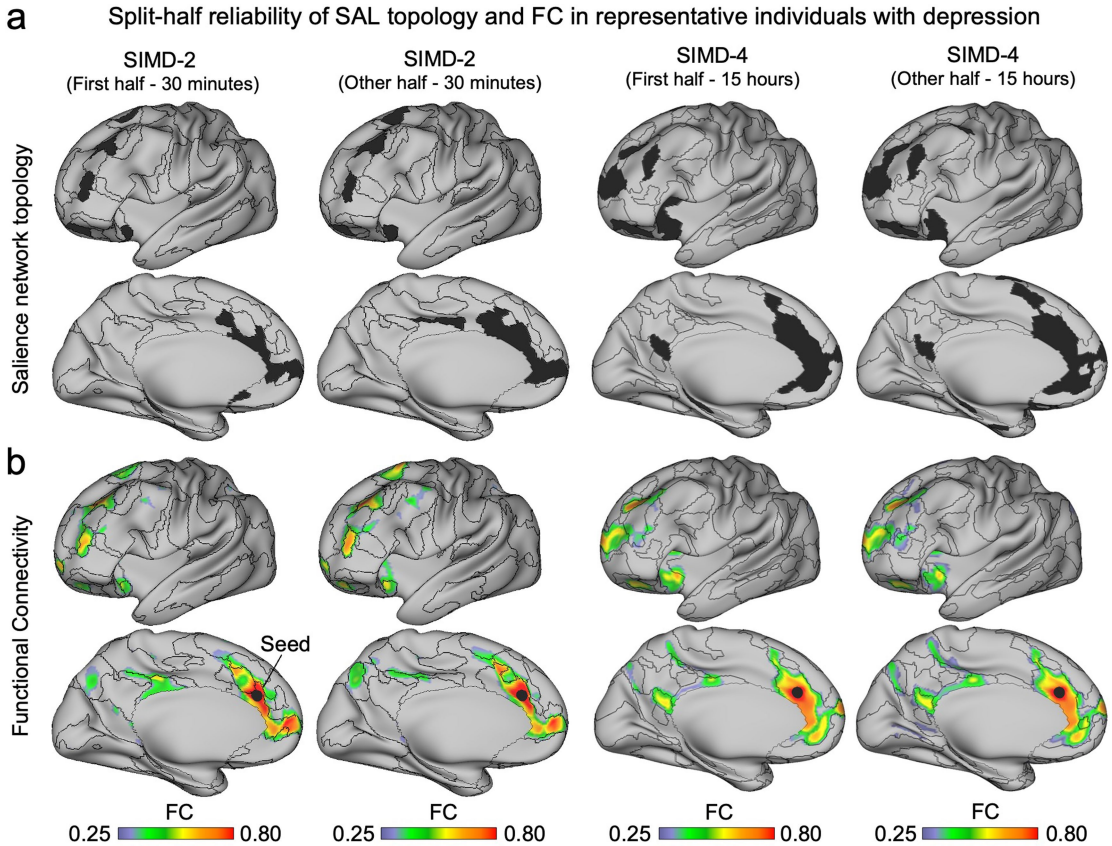

Extended Data Fig. 5 | Within-person stability of salience network topology and connectivity. a-b, Split-half reliability testing of salience network topology and functional connectivity in the least (SIMD-2, 58 min of fMRI scanning total) and most (SIMD-4, 29.96 hrs. of fMRI scanning total) sampled individuals with depression from the Serial Imaging of Major Depression (SIMD) dataset.

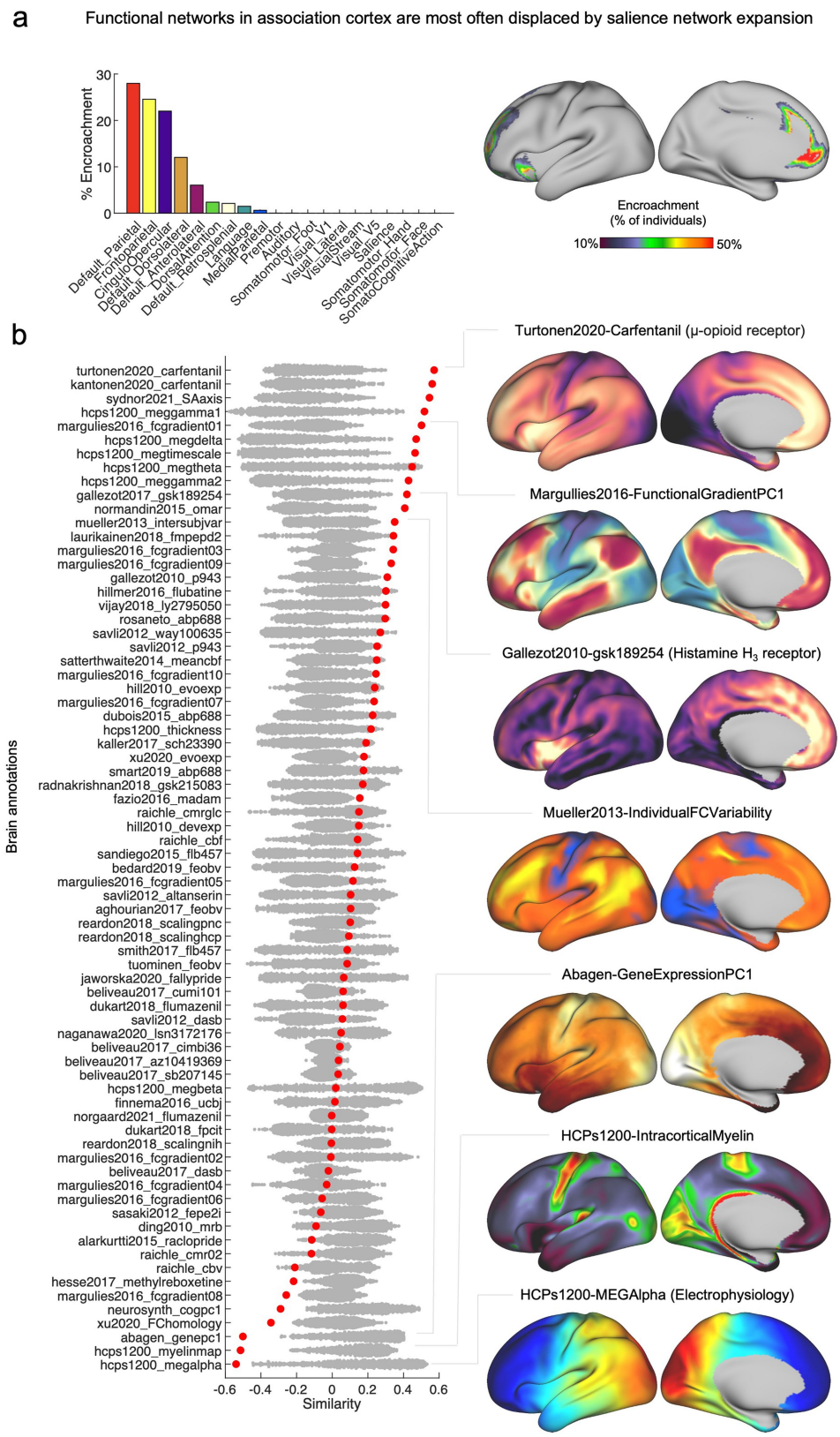

Extended Data Fig. 6 | See next page for caption.

Extended Data Fig. 6 | Salience network expansion in depression disproportionately affects heteromodal systems neighboring it, not unimodal sensorimotor networks. a, On average across subjects, the majority of salience network expansion in depression affected either the Default-parietal, Frontoparietal, or Cingulo-opercular networks. In contrast, Salience network encroachment upon unimodal sensorimotor networks (for example, the visual, auditory, somatomotor subnetworks) was absent. **b**, The average map of Salience network encroachment was compared to 73 canonical maps of the brain's functional and structural architecture ("annotations") obtained from the neuromaps toolbox[53] to help identify possible biological mechanisms for its expansion in individuals with depression. These maps are derived from a variety of independent molecular, microstructural, electrophysiological, developmental, and functional datasets. Spatial similarity was quantified using Spearman rank correlation, and statistical significance evaluated via spatial autocorrelation preserving null models. We observed multiple significant associations – including with principal gradients of functional connectivity and gene expression, and the spatial distribution of neurotransmitter receptors (μ-opioid, histamine H3 receptors), intracortical myelin, and individual variability in functional connectivity.

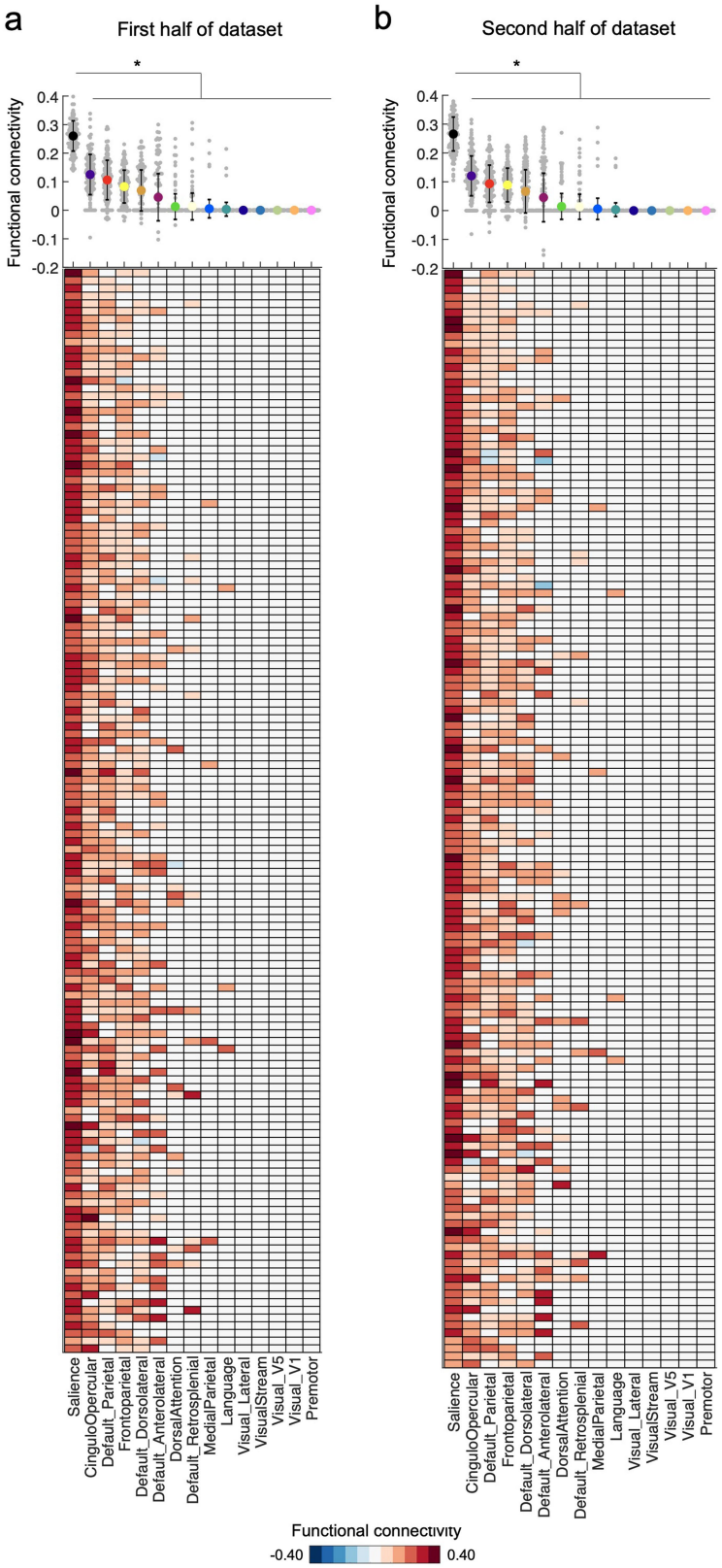

Extended Data Fig. 7 | See next page for caption.

Extended Data Fig. 7 | Salience network expansion in depression is associated with stable patterns of atypical functional connectivity. a-b, Evaluating functional connectivity strength between encroaching and non-encroaching vertices of the Salience network relative to runner-up network assignments network. Strength of functional connectivity between encroaching nodes of the salience network and the rest of the Salience network, and the functional networks that typically occupy that space in healthy controls (most often Default, Frontoparietal, or Cingulo-opercular). This analysis was performed using split halves of each individual's resting-state fMRI dataset to evaluate the stability of the Salience network assignment associated with the "encroaching" vertices relative to the runner-up assignments. Functional connectivity between encroaching Salience network vertices and the rest of the Salience network was on average 59% stronger than with the runner-up network (two-tailed independent sample t-test, all P's < 0.001, Bonferroni correction, n = 141). This was the case when using either the first (**a**) or second (**b**) half of each individual's concatenated resting-state fMRI dataset, indicating good stability. Error bars represent standard deviation.

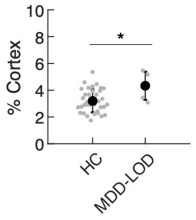

Extended Data Fig. 8 | Increased cortical representation of salience network in adults with late-onset depression. Five individuals (mean age = 66.60 ± 5.31 years, 5 F) with a diagnosis of major depression and met criteria for late-onset depression (LOD, defined here as onset of first depressive episode at or after the age of 60) underwent repeated clinical assessments and fMRI scans (6 × 10.64 min multi-echo resting-state fMRI scans, 63.84 min total per-subject) before, during, and after a brief evidence-based psychotherapy. Salience network was larger in these individuals with LOD relative to healthy controls (two-tailed permutation test, *P = 0.009, uncorrected, Z-score = 2.90). The n = 37 healthy control data are also shown in the main text Fig. 1c. Error bars represent standard deviation.

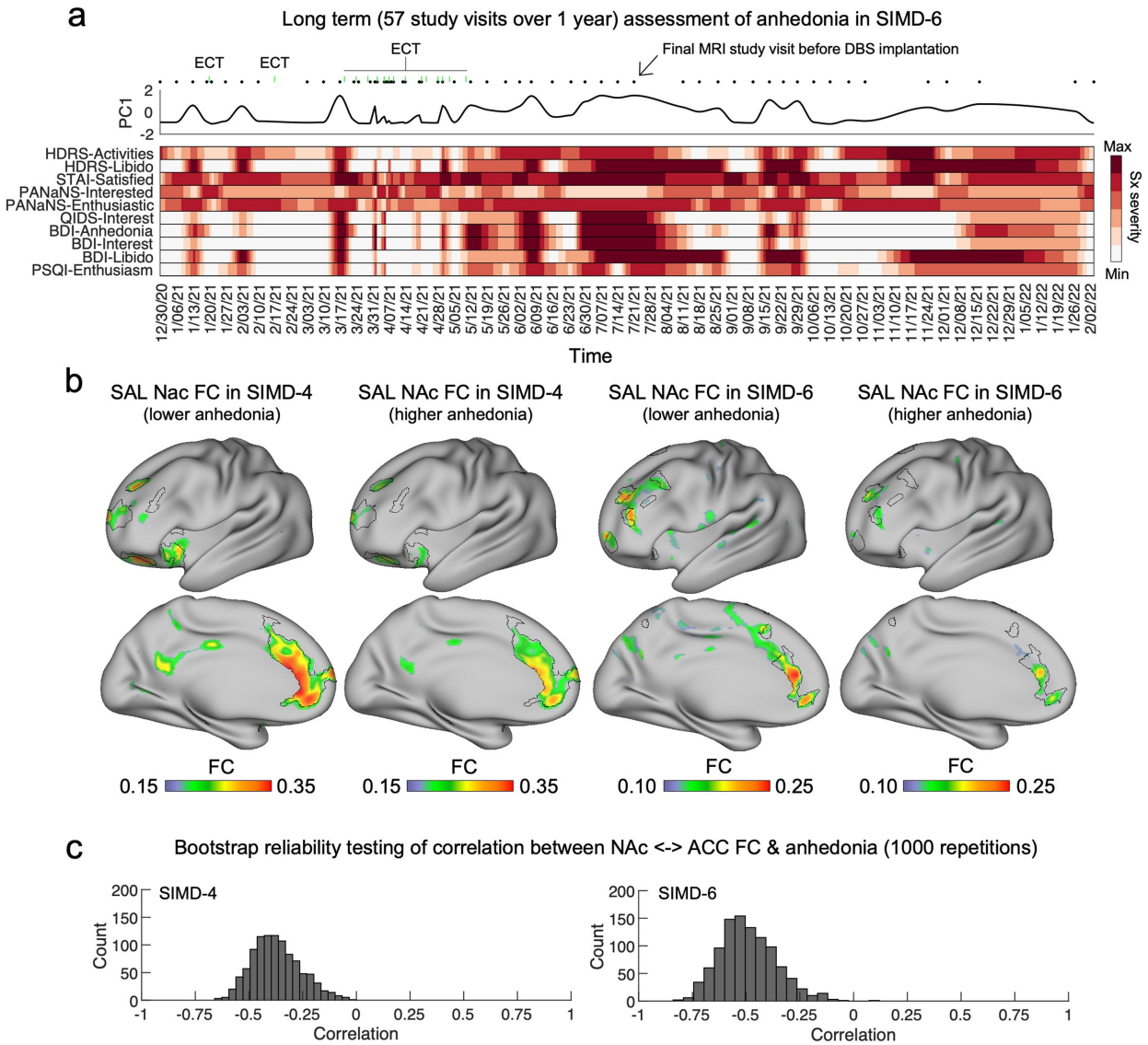

Extended Data Fig. 9 | Dense-sampling of depressive symptoms and functional connectivity in a second individual with depression. a, A heat map summarizes fluctuations in individual items selected from a variety of clinical interviews and self-report scales related to anhedonia in an example individual (SIMD-6). Clinical data was resampled (using shape- preserving piecewise cubic interpolation) to days for visualization purposes (black and red dots above heat map mark the dates of study visits and ECT treatments received unrelated to the present study, respectively). **b**, Functional connectivity of salience network voxels in nucleus accumbens (NAc) when symptoms of anhedonia are low (study visits in the bottom quartile) and high (study visits in top quartile). **c**, Bootstrap resampling (iteratively selecting 50% of all time points at random, and logging correlation between nucleus accumbens ←→ anterior cingulate FC and anhedonia) indicated good stability.

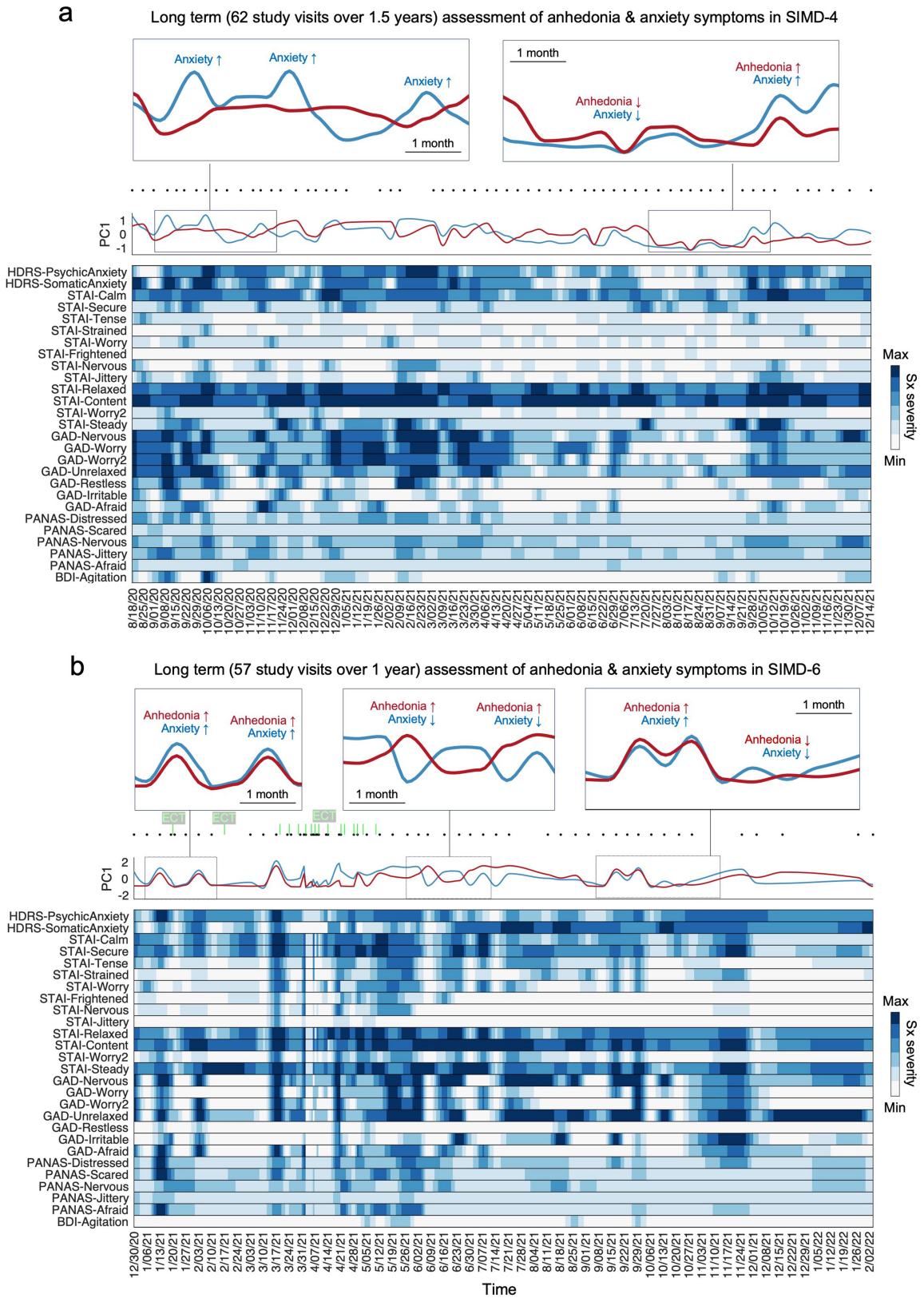

Extended Data Fig. 10 | Long term assessment of anhedonia and anxiety related symptoms in two deeply-sampled individuals with major depression. a-b, Heat map summarizes fluctuations in individual items related to anxiety (blue, 27 items total) that were selected from a variety of clinical interviews and self-report scales completed by two deeply-sampled individuals with depression (**a**, SIMD-4; **b**, SIMD-6). Head maps for anhedonia related items are shown in main text Fig. 4a and Extended Data Fig. 9a for SIMD-4 and SIMD-6, respectively. Clinical data was resampled (using shape-preserving piecewise cubic interpolation) to days for visualization purposes. The first principal component (PC1) of the anhedonia and anxiety measures were modestly correlated with one another within each individual over time (Pearson correlation, MDD04: $r = 0.41$, $P < 0.001$; MDD06: $r = 0.45$, $P < 0.001$), indicating that the severity of anxiety and anhedonia related symptoms can fluctuate independently of one another, but also that they both respond to global shifts in illness severity, which were primarily related to ECT in SIMD-6).

nature portfolio

Corresponding author(s): Charles Lynch Ph.D.
Conor Liston M.D., Ph.D.

Last updated by author(s): 5/30/2024

Reporting Summary

Nature Portfolio wishes to improve the reproducibility of the work that we publish. This form provides structure for consistency and transparency in reporting. For further information on Nature Portfolio policies, see our Editorial Policies and the Editorial Policy Checklist.

Statistics

For all statistical analyses, confirm that the following items are present in the figure legend, table legend, main text, or Methods section.

n/a	Confirmed	
☐	☒	The exact sample size (*n*) for each experimental group/condition, given as a discrete number and unit of measurement
☐	☒	A statement on whether measurements were taken from distinct samples or whether the same sample was measured repeatedly
☐	☒	The statistical test(s) used AND whether they are one- or two-sided *Only common tests should be described solely by name; describe more complex techniques in the Methods section.*
☐	☒	A description of all covariates tested
☐	☒	A description of any assumptions or corrections, such as tests of normality and adjustment for multiple comparisons
☐	☒	A full description of the statistical parameters including central tendency (e.g. means) or other basic estimates (e.g. regression coefficient) AND variation (e.g. standard deviation) or associated estimates of uncertainty (e.g. confidence intervals)
☐	☒	For null hypothesis testing, the test statistic (e.g. *F*, *t*, *r*) with confidence intervals, effect sizes, degrees of freedom and *P* value noted *Give P values as exact values whenever suitable.*
☒	☐	For Bayesian analysis, information on the choice of priors and Markov chain Monte Carlo settings
☒	☐	For hierarchical and complex designs, identification of the appropriate level for tests and full reporting of outcomes
☐	☒	Estimates of effect sizes (e.g. Cohen's *d*, Pearson's *r*), indicating how they were calculated

Our web collection on statistics for biologists contains articles on many of the points above.

Software and code

Policy information about availability of computer code

Data collection	No software was used for data collection.
Data analysis	Code for preprocessing multi-echo fMRI data is maintained in an online repository (https://github.com/cjl2007/Liston-Laboratory-MultiEchofMRI-Pipeline). Code for performing precision functional mapping and code specific to the analyses performed in this manuscript are maintained in an online repository (https://github.com/cjl2007/PFM-Depression). Software packages incorporated into the above pipelines for data analysis included: Matlab R2019a, https://www.mathworks.com/; Connectome Workbench 1.4.2, http://www.humanconnectome.org/software/connectome-workbench.html; Freesurfer v6, https://surfer.nmr.mgh.harvard.edu/; FSL 6.0, https://fsl.fmrib.ox.ac.uk/fsl/fslwiki; and Infomap v2.0.0, https://www.mapequation.org. Advanced Normalization Tools (ANTS; v2.3.4).

For manuscripts utilizing custom algorithms or software that are central to the research but not yet described in published literature, software must be made available to editors and reviewers. We strongly encourage code deposition in a community repository (e.g. GitHub). See the Nature Portfolio guidelines for submitting code & software for further information.

Data

Policy information about availability of data

All manuscripts must include a data availability statement. This statement should provide the following information, where applicable:

- Accession codes, unique identifiers, or web links for publicly available datasets
- A description of any restrictions on data availability
- For clinical datasets or third party data, please ensure that the statement adheres to our policy

Data from the Weill Cornell Multi-echo and Eskalibur datasets are available on reasonable request from C.J.L, I.E., J.D.P, C.L., and S.M., C.C.

Data from the MyConnectome dataset is available in the openneuro repository at https://openneuro.org/datasets/ds000031/versions/2.0.2.

Data from the Midnight Scan Club dataset is available in the openneuro repository at https://openneuro.org/datasets/ds000224/versions/1.0.4. Data from the Cast-induced plasticity dataset is available in the openneuro repository at https://openneuro.org/datasets/ds002766/versions/3.0.0.

Data from the Natural Scenes Dataset is available from Amazon Web Services (AWS) at https://registry.opendata.aws/nsd/.

The ABCD data used in this report are from Annual Release 5.0.

Data from individual subjects with depression are a part of ongoing clinical trials and not publicly available at this time.

Research involving human participants, their data, or biological material

Policy information about studies with human participants or human data. See also policy information about sex, gender (identity/presentation), and sexual orientation and race, ethnicity and racism.

Reporting on sex and gender	Findings apply to all studied individuals and groups, regardless of sex. Sex ratios: Serial imaging of Major Depression Dataset: 3M, 3F Weill Cornell Medicine rTMS 1 dataset: 21M, 27F Weill Cornell Medicine rTMS 2 dataset: 24M, 21F Stanford University rTMS dataset: 13M, 29 F Weill Cornell Late-onset Depression dataset: 0M, 5F Weill Cornell Multi-echo dataset: 7M, 0F MyConnectome dataset: 1M, 0F Midnight Scan Club: 5M, 5F Cast-induced plasticity dataset: 1M, 0F Natural Scenes Dataset: 2M, 6F Eskalibur dataset: 5M, 5F Sample selected from Adolescent Brain Cognitive Development study: 54M, 60F
Reporting on race, ethnicity, or other socially relevant groupings	No socially constructed or socially relevant categorization variables were used or are relevant for our manuscript.
Population characteristics	Findings apply to all studied individuals and groups, regardless of age. Age: Serial imaging of Major Depression Dataset: mean age = 29.47 ± 8.28 years Weill Cornell Medicine rTMS 1 dataset: mean age = 40.89 ± 12.73 years Weill Cornell Medicine rTMS 2 dataset: mean age = 44.46 ± 15.38 years Stanford University rTMS dataset: mean age = 38.09 ± 12.77 years Weill Cornell Late-onset Depression dataset: mean age = 66.60 ± 5.31 years Weill Cornell Multi-echo dataset: mean age = 33.42 ± 9 years MyConnectome dataset: 45 years-old Midnight Scan Club: mean age = 29.1 ± 3.3 years Cast-induced plasticity dataset: 27 years-old Natural Scenes Dataset: mean age = 26.50 ± 4.24 years Eskalibur dataset: mean age = 31.4 ± 5.4 years Adolescent Brain Cognitive Development dataset: 9.46 ± 0.50 years at baseline study visit
Recruitment	Serial imaging of Major Depression Dataset: Individuals with depression were recruited from the NYC metro area via flyers and word of mouth. Weill Cornell rTMS dataset: Individuals with depression were recruited from the NYC metro area via flyers and word of mouth. Stanford University rTMS dataset: Individuals with depression were recruited from the Bay area via flyers and word of mouth.

Weill Cornell Late-onset Depression dataset: Individuals with depression were recruited from the Bay area via flyers and word of mouth.
Weill Cornell Multi-echo dataset: Healthy adult subjects were recruited from the Weill Cornell Medical School community via word of mouth.
MyConnectome dataset: The subject in this dataset was also the principal investigator.
Midnight Scan Club: Healthy adult subjects were recruited from the Washington University community via flyers and word of mouth.
Cast-induced plasticity dataset: Healthy adult subjects were recruited from the Washington University community via flyers and word of mouth.
Natural Scenes Dataset: Participants were recruited through advertisements to the local community and were screened based on ability to participate in a neuroimaging study.
Eskalibur dataset: Participants were recruited through advertisements to the local community.
Adolescent Brain Cognitive Development dataset: Participants were recruited from a nationally distributed set of 21 study sites.

Ethics oversight

Serial imaging of Major Depression Dataset, Weill Cornell rTMS dataset, Stanford University rTMS dataset, Weill Cornell Late-onset Depression dataset, and Weill Cornell Multi-echo dataset: The study was approved by the Weill Cornell Medicine Institutional Review Board.
MyConnectome dataset: It was determined that this study did not meet requirements for human subjects research and thus that Institutional Review Board (IRB) approval was not necessary. Subsequent data collection at Washington University was collected under an approved IRB protocol.
Midnight Scan Club, Cast-induced plasticity dataset: These studies were approved by the Washington University School of Medicine Human Studies Committee and Institutional Review Board.
Natural Scenes Dataset: Participants were recruited through advertisements to the local community and were screened based on ability to participate in a neuroimaging study.
Eskalibur dataset: The study was approved by the local ethics committee.
Adolescent Brain Cognitive Development dataset: The ABCD Study obtained centralized institutional review board approval from the university of California, San Diego, and each of the 21 study sites obtained local institutional review board approval.

Note that full information on the approval of the study protocol must also be provided in the manuscript.

Field-specific reporting

Please select the one below that is the best fit for your research. If you are not sure, read the appropriate sections before making your selection.

☒ Life sciences ☐ Behavioural & social sciences ☐ Ecological, evolutionary & environmental sciences

For a reference copy of the document with all sections, see nature.com/documents/nr-reporting-summary-flat.pdf

Life sciences study design

All studies must disclose on these points even when the disclosure is negative.

Sample size	This study collected large quantities of data (repeated fMRI and clinical assessments) in individual subjects, and the majority of our analyses are conducted at the within-subject level. For these analyses, the relevant factor is having enough high quality data per-subject for reliable and accurate inferences. We and other groups (i.e., Laumann et al., 2015, Gordon et al., 2017, Lynch et al., 2020) have shown that approximately 30 minutes of resting-state fMRI data per-subject is necessary for reliable functional connectivity measurements, and we have at least that much data for each subject in our study.
Data exclusions	No subjects were excluded from analyses.
Replication	The main experimental findings (Figure 1c) were replicated (thrice) in held-out replication datasets, and in independent large n group-average datasets (Extended Data Figure 4). Brain-behavior relationships observed in individual subjects studied longitudinally (e.g., Figure 3, Figure 4) were replicated across multiple subjects.
Randomization	Experimental groups consisted of whether or not individual subjects had a diagnosis of major depression. Therefore, randomization is not possible.
Blinding	No blinding was performed.

Reporting for specific materials, systems and methods

We require information from authors about some types of materials, experimental systems and methods used in many studies. Here, indicate whether each material, system or method listed is relevant to your study. If you are not sure if a list item applies to your research, read the appropriate section before selecting a response.

Materials & experimental systems

n/a	Involved in the study
☒	☐ Antibodies
☒	☐ Eukaryotic cell lines
☒	☐ Palaeontology and archaeology
☒	☐ Animals and other organisms
☐	☒ Clinical data
☒	☐ Dual use research of concern
☒	☐ Plants

Methods

n/a	Involved in the study
☒	☐ ChIP-seq
☒	☐ Flow cytometry
☐	☒ MRI-based neuroimaging

Clinical data

Policy information about clinical studies

All manuscripts should comply with the ICMJEguidelines for publication of clinical research and a completedCONSORT checklist must be included with all submissions.

Clinical trial registration	NCT04041479; NCT04982757
Study protocol	Study overview is available online (NCT04041479: https://clinicaltrials.gov/study/NCT04041479#study-overview; NCT04982757: https://classic.clinicaltrials.gov/ct2/show/NCT04982757
Data collection	NCT04041479: Data was collected at Weill Cornell Medicine and Stanford University starting on 9/17/2021. NCT04982757: Data was collected at Weill Cornell Medicine starting on 7/29/2021. Data collection is ongoing as of 5/30/2024.
Outcomes	NCT04041479: Primary outcome is change in depression, as measured by the Hamilton Depression Rating Scale (HAMD17). Secondary outcome is change in depression, as measured by the Quick Inventory of Depressive Symptomatology (QIDS). The trial is ongoing, the trial's primary outcome measure was not analyzed in the present study. NCT04982757: Primary outcome is percent change in Montgomery-Asberg Depression Rating Scale (MADRS) scores for participants with treatment resistant depression [Time Frame: Baseline to Treatment End: Day 5 or 10 (depending on number of 5-day treatment courses administered)]. The MADRS is a measure of depression symptoms and is scored on a scale of 0 to 60, with 0 being no depressive symptoms and 60 being severe depressive symptoms. The secondary outcome measure is Percent Change in Quick Inventory of Depressive Symptomatology (QIDS) scores for participants with OCD [Time Frame: Baseline to Treatment End: Day 5 or 10 (depending on number of 5-day treatment courses administered)]. The QIDS is a self-report measure of depression symptoms and is scored on a scale of 0 to 27, with 0 being no depressive symptoms and 27 being severe depressive symptoms. The trial is ongoing, the trial's primary outcome measure was not analyzed in the present study.

Magnetic resonance imaging

Experimental design

Design type	Resting-state fMRI
Design specifications	Resting-state fMRI: 47 to 1,792 minutes of data per-subject
Behavioral performance measures	Behavioral outputs were not recorded.

Acquisition

Imaging type(s)	Structural, Functional.
Field strength	3T, 7T
Sequence & imaging parameters	Serial Imaging of Major Depression dataset: MRI data were acquired on a Siemens Magnetom Prisma 3T scanner at the Citigroup Biomedical Imaging Center of Weill Cornell's medical campus using a Siemens 32-channel head coil. Multi-echo, multi-band resting-state fMRI scans were collected using a T2*-weighted echo-planar sequence covering the full brain (TR: 1355 ms; TE1: 13.40 ms, TE2: 31.11 ms, TE3: 48.82 ms, TE4: 66.53 ms, and TE5: 84.24 ms; FOV: 216 mm; flip angle: 68° (the Ernst angle for gray matter assuming a T1 value of 1400 ms); 2.4 mm isotropic voxels; 72 slices; AP phase encoding direction; in-plane acceleration factor: 2; and multi-band acceleration factor: 6) with 640 volumes acquired per scan for a total acquisition time of 14 minutes and 27 seconds. Spin echo EPI images with opposite phase encoding directions (AP and PA) but identical geometrical parameters and echo spacing were acquired before each resting-state scan. Multi-echo T1-weighted (TR/TI: 2500/1000 ms; TE1: 1.7 ms, TE2: 3.6 ms, TE3: 5.5 ms, TE4: 7.4 ms ; FOV: 256 mm; flip angle: 8°, and 208 sagittal slices with a 0.8 mm slice thickness) and T2-weighted anatomical images (TR: 3200 ms; TE: 563 ms; FOV: 256; flip angle: 8°, and 208 sagittal slices with a 0.8 mm slice thickness) were also collected. Weill Cornell rTMS dataset: MRI data were acquired on a Siemens Magnetom Prisma 3T machine at the Citigroup Biomedical Imaging Center of Weill Cornell's medical campus using a Siemens 32-channel head coil. Multi-echo, multi-

band resting-state fMRI scans were collected at each study visit using a T2*-weighted echo-planar sequence covering the full brain (TR: 1300 ms; TE1: 12.60 ms, TE2: 29.51 ms, TE3: 46.42 ms, and TE4: 63.33 ms; FOV: 216 mm; flip angle: 67° (the Ernst angle for gray matter assuming a T1 value of 1400 ms); 2.5 mm isotropic voxels; 60 slices; AP phase encoding direction; in-plane acceleration factor: 2; and multi-band acceleration factor: 4) with 650 volumes acquired per scan for a total acquisition time of 14 minutes and 5 seconds. Spin echo EPI images with opposite phase encoding directions (AP and PA) but identical geometrical parameters and echo spacing were acquired before each resting-state scan. Multi-echo T1-weighted (TR/TI: 2500/1000 ms; TE1: 1.7 ms, TE2: 3.6 ms, TE3: 5.5 ms, TE4: 7.4 ms ; FOV: 256; flip angle: 8°, and 208 sagittal slices with a 0.8 mm slice thickness) and T2-weighted anatomical images (TR: 3200 ms; TE: 563 ms; FOV: 256; flip angle: 8°, and 208 sagittal slices with a 0.8 mm slice thickness) were also collected.

Stanford University rTMS dataset: MRI data were acquired on a GE SIGNA 3T machine at the Center for Neurobiological Imaging on Stanford University's campus using a Nova Medical 32-channel head coil. Multi-echo, multi-band resting-state fMRI scans were collected using a T2*-weighted echo-planar sequence covering the full brain (TR: 1330 ms; TE1: 13.7 ms, TE2: 31.60 ms, TE3: 49.50 ms, and TE4: 67.40 ms; flip angle: 67° (the Ernst angle for gray matter assuming a T1 value of 1400 ms); 3 mm isotropic voxels; 52 slices; AP phase encoding direction; in-plane acceleration factor: 2; and multi-band acceleration factor: 4) with 338 volumes acquired per scan for a total acquisition time of 7 minutes and 30 seconds. Spin echo EPI images with opposite phase encoding directions (AP and PA) but identical geometrical parameters and echo spacing were acquired before each resting-state scan.T1-weighted and T2-weighted anatomical images were also collected.

Weill Cornell Late-onset Depression dataset: MRI data were acquired on a Siemens Magnetom Prisma 3T machine at the Citigroup Biomedical Imaging Center of Weill Cornell's medical campus using a Siemens 32-channel head coil. Multi-echo, multi-band resting-state fMRI scans were collected at each study visit using a T2*-weighted echo-planar sequence covering the full brain (TR: 1300 ms; TE1: 12.60 ms, TE2: 29.51 ms, TE3: 46.42 ms, and TE4: 63.33 ms; FOV: 216 mm; flip angle: 67° (the Ernst angle for gray matter assuming a T1 value of 1400 ms); 2.5 mm isotropic voxels; 60 slices; AP phase encoding direction; in-plane acceleration factor: 2; and multi-band acceleration factor: 4) with 480 volumes acquired per scan for a total acquisition time of 10 minutes and 38 seconds. Spin echo EPI images with opposite phase encoding directions (AP and PA) but identical geometrical parameters and echo spacing were acquired before each resting-state scan. Multi-echo T1-weighted (TR/TI: 2500/1000 ms; TE1: 1.7 ms, TE2: 3.6 ms, TE3: 5.5 ms, TE4: 7.4 ms ; FOV: 256 mm; flip angle: 8°, and 208 sagittal slices with a 0.8 mm slice thickness) and T2-weighted anatomical images (TR: 3200 ms; TE: 563 ms; FOV: 256; flip angle: 8°, and 208 sagittal slices with a 0.8 mm slice thickness) were also acquired.

Area of acquisition: Whole-brain

Diffusion MRI ☐ Used ☒ Not used

Preprocessing

Preprocessing software: Preprocessing of multi-echo data minimized spatial interpolation and volumetric smoothing while preserving the alignment of echoes. The single-band reference (SBR) images (one per echo) for each scan were averaged. The resultant average SBR images were aligned, averaged, co-registered to the ACPC aligned T1-weighted anatomical image, and simultaneously corrected for spatial distortions using FSL's topup and epi_reg programs. Freesurfer's bbregister algorithm was used to refine this co-registration. For each scan, echoes were combined at each timepoint and a unique 6 DOF registration (one per volume) to the average SBR image was estimated using FSL's MCFLIRT tool, using a 4-stage (sinc) optimization. All of these steps (co-registration to the average SBR image, ACPC alignment, and correcting for spatial distortions) were concatenated using FSL's convertwarp tool and applied as a single spline warp to individual volumes of each echo after correcting for slice time differences using FSL's slicetimer program. The functional images underwent a brain extraction using the co-registered brain extracted T1-weighted anatomical image as a mask and corrected for signal intensity inhomogeneities using ANT's N4BiasFieldCorrection tool.

Software packages incorporated into the preprocessing pipelines included: Matlab R2019a, https://www.mathworks.com/; Connectome Workbench 1.4.2, http://www.humanconnectome.org/software/connectome-workbench.html; Freesurfer v6, https://surfer.nmr.mgh.harvard.edu/; FSL 6.0, https://fsl.fmrib.ox.ac.uk/fsl/fslwiki; and Infomap, https://www.mapequation.org.

Normalization: T1w ---> atlas linear, BOLD --> atlas.

Normalization template: MNI

Noise and artifact removal: Preprocessed multi-echo data were submitted to multi-echo ICA (ME-ICA), which is designed to isolate spatially structured T2*- (neurobiological; "BOLD-like") and S0-dependent (non-neurobiological; "not BOLD-like") signals and implemented using the "tedana.py" workflow 65. In short, the preprocessed, ACPC-aligned echoes were first combined according to the average rate of T2* decay at each voxel across all time points by fitting the monoexponential decay, S(t) = S0e -t / T2* . From these T2* values, an optimally-combined multi-echo (OC-ME) time-series was obtained by combining echoes using a weighted average (WTE = TE * e -TE/ T2*). The covariance structure of all voxel time-courses was used to identify major signals in the OC-ME time-series using principal component and independent component analysis. Components were classified as either T2*-dependent (and retained) or S0-dependent (and discarded), primarily according to their decay properties across echoes. All component classifications were manually reviewed by author CJL and revised when necessary. Mean gray matter time-series regression was performed to remove spatially diffuse noise. Temporal masks were generated for censoring high motion time-points using a framewise displacement (FD) threshold of 0.3 mm and a backward difference of two TRs, for an effective sampling rate comparable to historical FD measurements (approximately 2 to 4 seconds). Prior to the FD calculation, head realignment parameters were filtered using a stopband Butterworth filter (0.2 - 0.35 Hz) to attenuate the influence of

respiration on motion parameters. Single-echo fMRI datasets (e.g., NSD, ABCD) were subjected to the same preprocessing procedures, except ICA-AROMA was used instead of ME-ICA.

Volume censoring: See above.

Statistical modeling & inference

Model type and settings: We measured the surface area (in mm2) that each vertex in the individual's midthickness surface is responsible for ("wb_command --surface-vertex-areas"). Next, we calculated the relative contribution (size) of each functional network to the total cortical surface area by taking the total surface area of all network vertices in relation to the total cortical surface area. In the striatum, where each voxel represents the same amount of tissue, the relative contribution of each functional network to the total striatal volume was calculated by taking the total number of network voxels in relation to the total striatal voxels.The statistical significance of group differences in network size were evaluated using permutation tests and independent sample t-tests (the latter implemented using Matlab's ttest2.m function). Effect size (Cohen's d) was calculated as difference in group means divided by pooled standard deviation. Assumptions regarding equal variance were adjusted when appropriate (based on two-sample F-tests performed using Matlab's vartest2.m function). The relative difference between groups was calculated as the absolute difference divided by network size in healthy controls.

Effect(s) tested: With respect to testing differences in functional network size, permutation and independent sample t-tests tested against null hypothesis that difference in group means is zero.

Specify type of analysis: ☐ Whole brain ☒ ROI-based ☐ Both

Anatomical location(s): Individual-specific functional networks were created from each individual's resting-state fMRI data.

Statistic type for inference (See Eklund et al. 2016): No cluster wise inferences were made.

Correction: P-values were adjusted using Bonferroni correction for multiple comparisons.

Models & analysis

n/a	Involved in the study
☐	☒ Functional and/or effective connectivity
☐	☒ Graph analysis
☐	☒ Multivariate modeling or predictive analysis

Functional and/or effective connectivity: Pearson correlation.

Graph analysis: Individual-specific (and in some cases, group-average) functional networks were identified using the procedures described in Gordon et al., 2020 PNAS and Lynch et al., 2022 Neuron. A functional connectivity matrix summarizing the correlation between the time-courses of all cortical vertices and subcortical voxels across all study visits was constructed. Correlations between nodes ≤ 10 mm apart (geodesic and Euclidean space used for cortico-cortical and subcortical-cortical distance, respectively) were set to zero. Correlations between voxels belonging to subcortical structures were set to zero. Functional connectivity matrices were thresholded in such a way that they retained at least the strongest X% correlations (0.01, 0.02, 0.05, 0.1, 0.2, 0.5, 1, 2, and 5%) to each vertex and voxel and were used as inputs for the InfoMap community detection algorithm. Free parameters (for example, the number of algorithm repetitions) for the Infomap algorithm were fixed across subjects. The optimal scale for further analysis across individuals was defined as the graph threshold producing the best size-weighted average homogeneity relative to the median of the size-weighted average homogeneity calculated from randomly rotated networks. Size-weighted average homogeneity was maximized relative to randomly rotated communities at the 0.1% graph density. Each Infomap community was algorithmically assigned to one of 20 possible functional network identities (Default-Parietal, Default-Anterolateral, Default-Dorsolateral, Default-Retrosplenial, Visual-Lateral, Visual-Stream, Visual-V1, Visual-V5, Frontoparietal, Dorsal Attention, Premotor / Dorsal Attention II, Language, Salience, Cingulo-opercular / Action-mode, Parietal memory, Auditory, Somatomotor-Hand, Somatomotor-Face, Somatomotor-Foot, Auditory, or Somato-Cognitive-Action) primarily according their functional connectivity and spatial locations relative to a specified set of priors. This procedure is implemented using a Matlab function ("pfm_identify_networks.m") available on our study's GitHub repository (https://github.com/cjl2007/PFM-Depression). The priors used in our study ("Priors.mat") are also available in the same repository. All algorithmic assignments were manually reviewed by study author CJL and manually adjusted in the case of an ambiguous assignment.

Multivariate modeling and predictive analysis: A support vector machine classifier, where class labels were diagnosis status (healthy control or depression) and features were functional brain network size in each individual, was trained using repeated (100 iterations) nested split-half (2-fold) cross-validation with a grid search optimization strategy for hyperparameter tuning (box constraint, kernel size). Classification accuracy was calculated as the percentage of correct predictions, and statistical significance assessed using permutation tests. Confusion matrix was created using Matlab's confmat.m function. Feature importance was evaluated by iteratively omitting each functional network and calculating the resulting loss in accuracy. The Synthetic Minority Oversampling Technique (SMOTE) was used to prevent classification bias in favor of the majority class, and performed on

training data only to avoid data leakage.